JGR Atmospheres

RESEARCH ARTICLE
10.1029/2025JD045348

Dynamic Versus Diabatic Controls on Atmospheric Variability in a Tropical Aquachannel

Hyunju Jung[1] and **Peter Knippertz**[1]

[1]Institute of Meteorology and Climate Research Troposphere Research (IMKTRO), Karlsruhe Institute of Technology, Karlsruhe, Germany

Key Points:

- Atmospheric variability in tropical aquachannel simulations is highly sensitive to model resolution and convective treatment
- The tested model configurations mainly differ by varying contributions from dynamical Kelvin waves and diabatically forced standing waves
- The interaction between the two with the largest wind shear support the formation of a Madden-Julian Oscillation-like disturbance

Supporting Information:

Supporting Information may be found in the online version of this article.

Correspondence to:

P. Knippertz,
peter.knippertz@kit.edu

Citation:

Jung, H., & Knippertz, P. (2026). Dynamic versus diabatic controls on atmospheric variability in a tropical aquachannel. *Journal of Geophysical Research: Atmospheres*, *131*, e2025JD045348. https://doi.org/10.1029/2025JD045348

Received 5 SEP 2025
Accepted 6 JUN 2026

Author Contributions:

Conceptualization: Hyunju Jung, Peter Knippertz
Data curation: Hyunju Jung
Formal analysis: Hyunju Jung
Funding acquisition: Peter Knippertz
Investigation: Hyunju Jung, Peter Knippertz
Methodology: Hyunju Jung, Peter Knippertz
Project administration: Peter Knippertz
Resources: Hyunju Jung
Software: Hyunju Jung
Supervision: Peter Knippertz
Validation: Hyunju Jung
Visualization: Hyunju Jung
Writing – original draft: Hyunju Jung
Writing – review & editing: Hyunju Jung, Peter Knippertz

Abstract Synoptic- to planetary-scale atmospheric variability in the tropics is a potential source of predictability worldwide. However, current weather prediction models struggle to fully capture this variability. Here, we conduct tropical aquachannel simulations using the ICOsahedral Nonhydrostatic model with horizontal grid spacings of 13 and 5 km, and different representations of deep and shallow convection. The channel is confined between 30°N and 30°S with zonally symmetric sea surface temperatures prescribed. All aquachannel runs exhibit prominent Kelvin wave (KW) activity. The 13-km run with parameterized deep and shallow convection is characterized by KWs with propagation speeds varying between 15 and 27 m s^{-1}. Only this run, the background flow of which markedly differs from the others, produces a slowly eastward-propagating disturbance (SED) that resembles the Madden-Julian Oscillation with off-equatorial Rossby gyres. The other aquachannel runs exhibit wavenumber-one KWs with an almost constant propagation speed of 24 m s^{-1} superposed on quasi-standing or slowly drifting waves with much higher zonal wavenumbers. In runs with explicit deep convection, these quasi-standing waves are primarily controlled by the vertical advection of moist static energy, while in the 5-km run with parameterized deep and shallow convection, cloud-radiative effects play a bigger role. The latter are also key to maintaining the SED in the 13-km run with parameterized deep and shallow convection. This study demonstrates that subtle changes in model configuration can shift the large-scale atmospheric variability in the tropics between standing and propagating types of waves, which would greatly influence possible interactions with the extratropics.

Plain Language Summary Weather patterns in the tropical regions are strongly modulated by atmospheric waves, which are important for making more accurate weather forecasts throughout the world. Using a simplified modeling framework, we perform simulations of the tropical atmosphere with different grid sizes and methods for representing clouds and thunderstorms. Our simulations reveal a wide range of different behaviors shaped by a mixture of large-scale waves moving eastward at 5–27 m s^{-1} and smaller-scale waves that remain stationary. The latter are controlled by how energy is transported through the atmosphere and how clouds interacted with sunlight and heat emitted from the Earth's surface. One model configuration shows a prominent slow-moving, large-scale disturbance, apparently enabled by interactions between the cloud effects and the mechanisms of wave propagation. Overall, our research demonstrates the challenge of realistically representing tropical weather patterns in forecast models with potentially important implications for global weather predictions.

1. Introduction

Despite overall improvements in numerical weather prediction (NWP) in recent decades (Bauer et al., 2015), weather forecasts in the tropics, in particular of precipitation remain challenging (Haiden et al., 2012; Privé & Errico, 2013; Vogel et al., 2020). One reason for this is the difference in large-scale dynamics between the tropics and the extratropics. In the latter, geostrophic balance governs the synoptic-scale atmospheric circulation (Holton, 2004). In the tropics, however, the Coriolis force is too small and large solar insolation elevates the importance of thermodynamic processes such as moist convection (Raymond et al., 2015). Consequently, weather patterns in the tropics are primarily controlled by interactions of convection with synoptic- to planetary waves.

The tropics are characterized by different modes of variability on time scales from days to months. This variability is mostly related to equatorial waves (EWs; Kiladis et al., 2009) and the Madden-Julian Oscillation (MJO; Madden & Julian, 1971, 1972). EWs are east- or westward propagating disturbances trapped in the equatorial region, which are often coupled to deep convection and thus control a considerable fraction of tropical rainfall

variability (Takayabu, 1994; Yasunaga & Mapes, 2012). The theoretical characteristics of EWs can be derived from the shallow water equations on an equatorial beta plane (Matsuno, 1966). The MJO is a planetary-scale disturbance that slowly propagates eastward (~5 m s^{-1}) and is characterized by an intraseasonal time scale (30–90 days). Its large-scale pattern consists of an enhanced rainfall (or convection) phase and a suppressed rainfall phase (C. Zhang, 2005). Although extensive research on the MJO has been conducted in the last decades, there is no consensus on a theory for the MJO (C. Zhang et al., 2020). One of the proposed explanations is the moisture mode theory, in which prognostic moisture governs the evolution of dynamics (Adames & Kim, 2016). Applied to the MJO it implies that the intraseasonal variability of precipitation is predominantly driven by moisture fluctuations with cloud-radiative feedbacks further creating instability (Raymond, 2001). Beyond their structural characteristics, the MJO and EWs serve as primary drivers of subseasonal predictability, with the MJO exerting broad influence on global weather patterns (H.-M. Kim et al., 2014; Jiang et al., 2020). EWs offer a distinct predictive window of one to 2 weeks or possibly longer (Judt, 2020; Li & Stechmann, 2020; Ruckstuhl et al., 2026; Ying & Zhang, 2017) that may be extended through their interactions with the MJO (Adames & Wallace, 2014).

Despite their ubiquity in the tropics and their importance for predictability, weather prediction models often struggle to capture EWs and the MJO (Bengtsson et al., 2019; Dias et al., 2018). Idealized modeling approaches such as aquaplanet simulations reveal that tropical variability is highly sensitive to model configuration. A model intercomparison project of aquaplanet simulations showed that the behavior of EWs depends on the employed atmospheric model (Blackburn et al., 2013) and the prescribed SST pattern (Williamson et al., 2013). In such idealized configurations, EWs are also impacted by model geometry (aquaplanet, aquachannel or aquapatch) (Blanco, Nolan, & Tulich, 2016; Nakajima et al., 2013). The treatment of deep and shallow convection also affects the spectrum of variability (Rios-Berrios et al., 2022). Also, the characteristics of the MJO are sensitive to free-tropospheric moisture (Grabowski, 2003), moisture exchange between the surface and the boundary layer (Shi et al., 2018), or vertical resolution which is crucial for representing a realistic distribution of cloud types (Inness et al., 2001). While these studies utilized aquaplanet simulations with zonally symmetric SSTs, other idealized experiments highlight the importance of realistic SST distribution (H. Kim, 2024; H. Kim & Benedict, 2023), particularly since the eastward propagation of deep convection is often confined to the Indo-Pacific warm pool (C. Zhang, 2005). Furthermore, wave characteristics depend strongly on the background zonal flow, for example through Doppler-shifting (Yang et al., 2003). S. Tulich and Kiladis (2021) further demonstrated that shear in the background flow can affect waves through eddy forcing and modulation. Thus, wave characteristics can change substantially when a modification in a model alters the simulated mean state of the atmosphere.

A fundamental challenge in representing tropical variability lies in capturing the multi-scale interactions between large-scale circulation and organized convection (Randall, 2013; Tomassini, 2020). Observational studies have long identified a hierarchical structure where deep convection is organized into discrete entities: Cloud clusters on the mesoscale (several 100 km, 1–2 days) are often embedded within superclusters on the synoptic scale (several 1,000 km, 10 days) (Lau et al., 1991; Mapes & Houze, 1993; Nakazawa, 1988). These superclusters are frequently identified as the envelope of convectively coupled equatorial waves (Takayabu, 1994), most notably convectively coupled Kelvin waves (Wheeler & Kiladis, 1999). Within these envelopes, the mesoscale cloud clusters often manifest as westward intertio-gravity waves of the first meridional mode (WIG1) (S. S. Chen et al., 1996). While the wave-centric perspective is dominant, these organized convective systems are not always coupled to the underlying wave dynamics (Blanco, Nolan, & Mapes, 2016; Jung & Knippertz, 2023; S. N. Tulich & Kiladis, 2012; Yamasaki, 2011).

There have been successful efforts to improve this interaction, including increased sensitivity of convective entrainment to the environmental humidity (Bechtold et al., 2008), enhanced subgrid organization of convection (Bengtsson et al., 2021) and the explicit representation of convection in high-resolution simulations (Judt & Rios-Berrios, 2021; Miura et al., 2007). However, employing a similar approach in a different model does not necessarily ensure the same outcome. For example, explicit convection can, in some cases, deteriorate the propagation speed and amplitude of the MJO (Wedi et al., 2020) or bring no significant improvement in simulating tropical variability (Jung & Knippertz, 2023).

A radiative convective equilibrium (RCE) framework offers another valuable approach to investigate the intricate coupling between convection and larger-scale circulations (Manabe & Strickler, 1964). Within this framework, convective self-aggregation is defined as a spontaneous organization of convection into one or more localized

clusters on tropical SSTs despite homogeneous initial and boundary conditions (Bretherton et al., 2005; Tompkins & Craig, 1998). This aggregation emerges from positive feedback in which enhanced longwave radiative cooling in dry patches drives subsidence, further drying these regions and amplifying a larger-scale circulation that funnels moisture into active convective areas (Coppin & Bony, 2015; Holloway et al., 2017). While RCE simulations often omit planetary rotation, leading typically to standing organized clusters (Wing et al., 2020), some studies incorporate the Coriolis force, revealing important similarities between convective self-aggregation and the MJO such as slow eastward propagation (Arnold & Randall, 2015; Khairoutdinov & Emanuel, 2018). In contrast, convective self-aggregation exhibits significant persistence to external forcings. For example, an embedded background mean flow can initially induce propagation, but an organized system quickly restores a motionless state by adjusting surface momentum fluxes (Jung et al., 2021).

This manuscript investigates in depth how wave characteristics change due to different model configurations, specifically focusing on horizontal resolution and the treatment of deep and shallow convection. To isolate the role of tropical atmospheric dynamics and thermodynamics, we employ a tropical aquachannel framework. This idealized geometry allows us to circumvent the complexities associated with orography, land-sea contrasts, and tropical-extratropical interactions that are present in more realistic setups. While global aquaplanet simulations are useful for studying global circulation, their computational expense at high resolutions often precludes the detailed process-level investigations of equatorial waves and the MJO that our study requires. Conversely, aquapatch simulations, albeit computationally efficient, are suboptimal for investigating zonally propagating waves due to distorting zonal boundary conditions and limited zonal extent. Furthermore, our aquachannel framework is a modern setup compared to other aquachannel studies. For example, we feature a zonal extent equal to the Earth's circumference at the equator, which is longer than that in Bretherton and Khairoutdinov (2015), and use a horizontal resolution higher than Blanco, Nolan, & Tulich (2016). This enhanced configuration enables us to quantify the impact of model configuration on tropical wave characteristics in a more realistic setting.

Section 2 describes our model setup of the tropical channel simulations and the methods to identify different modes of variability. Section 3 presents the results of tropical variability and compares different wave characteristics due to model configuration. We discuss these results in Section 4 and provide our conclusions in Section 5.

2. Model and Methods

2.1. Aquachannel Simulations

For all simulations, we use version 2.6.3 of the ICOsahedral Nonhydrostatic (ICON) model (Zängl et al., 2015) in the NWP configuration. Before zooming in on the aquachannel, we run a sequence of aquaplanet simulations with the deep and shallow convection schemes described in Bechtold et al. (2008); Tiedtke (1989). The number of vertical levels is 90 with a model top at 75 km. SSTs are prescribed and follow a zonally symmetric pattern with a maximum of 27°C at the equator, which is equivalent to the Qobs profile in Neale and Hoskins (2000). We also use a fully non-linear Coriolis parameter and a fixed equinoctial diurnal cycle in solar insolation. The aquaplanet simulations are performed with a horizontal grid spacing of 40 km for 120 simulation days, after which the grid spacing is reduced to 26 km for another 90 days. After that, the simulation domain is confined to a tropical channel geometry between 30°N and 30°S. The boundary conditions for these latitudinal walls are obtained from the time-zonal average of virtual potential temperature, water vapor mixing ratio, air density, and zonal and vertical winds in the 26-km aquaplanet simulation. These time-invariant quantities are prescribed for the 13-km aquachannel simulation. Other meteorological variables are set to zero, for example, meridional wind is prescribed to be zero at 30°N and 30°S. These prescribed latitudinal walls isolate tropical processes by excluding extratropical interactions. Since our study focuses on equatorially trapped waves that decay significantly before reaching the boundaries, the lateral walls do not affect the wave dynamics. Furthermore, all diagnostic analyses are performed strictly on the interior domain between 20°N and 20°S to ensure that results are not influenced by potential numerical artifacts or artificial diffusion near the walls. The succession of aquaplanet simulations is to spin up the aquachannel simulation and to obtain boundary conditions for the latitudinal walls.

The aquachannel simulation is initialized with the last time step of the 26-km aquaplanet run. The simulation setup otherwise remains identical, except for the finer horizontal grid spacing of 13 km and different convective treatments in some runs. Table 1 summarizes important differences between the aquachannel simulations. In total, we performed four 13-km aquachannel simulations: P13 uses the same deterministic parameterization schemes

Table 1
Horizontal Grid Spacing and Treatment of Deep and Shallow Convection for Each Experiment

Exp. name	Δx [km]	Deep conv.	Shallow conv.
P13	13	On	On (deterministic)
E13	13	Off	Off
S13	13	Off	On (deterministic)
SS13	13	Off	On (stochastic)
P5	5	On	On (deterministic)
E5	5	Off	Off

for deep and shallow convection as the aquaplanet simulations. E13 represents deep and shallow convection explicitly. Note that full convection parameterizations are typically recommended for model configurations with horizontal grids exceeding 5 km (Prill et al., 2024). S13 uses the deterministic scheme for shallow convection with explicitly representing deep convection, while SS13 replaces the shallow convection scheme with a stochastic version (Sakradzija et al., 2015, 2020). All runs are performed for 102 simulation days with a spin-up of 62 days and an analysis period of 40 days.

We also performed two 5-km aquachannel simulations, which are initialized from the last time step of P13. Compared to P13, the only change for P5 is the horizontal grid spacing, while E5 explicitly represents deep and shallow convection at 5 km. The spin-up is longer for E5 (5 days) than for P5 (3 days), since the subtle modification of grid spacing allows P5 to transit more smoothly from P13. After the spin-up, both 5-km runs have a 40-day analysis period consistent with the coarser-resolution runs. A full description of the model setup and configuration can be found in Jung et al. (2023). For the remaining of the manuscript, we investigate the full 40-day analysis period with its beginning referred to as day 0. The model outputs are coarsened to a 0.2° latitude-longitude grid using conservative remapping.

2.2. Identification of Equatorial Waves

To distinguish coherent wave dynamics from non-wave-type cloud clusters, this study identifies EWs. For that, we use two different wave filtering tools to identify waves: (a) rainfall is filtered using narrow wavenumber-frequency window for specific wave types (Wheeler & Kiladis, 1999, hereafter WK), and (b) horizontal winds and geopotential height at 200 hPa are projected onto horizontal structures of waves (Yang et al., 2003, hereafter YP). These two approaches are sensitive to different wave characteristics. WK emphasizes the circum-equatorial propagation behavior of a moist wave, whereas YP emphasizes the agreement of simulated horizontal patterns in wind and geopotential with the wave theory based on a shallow-water system. WK is generally applicable to a wide range of scalar data such as rainfall, infrared brightness temperature and other fields related to convective clouds (Yasunaga & Mapes, 2012). WK can also isolate the characteristic wavenumbers and frequencies of the MJO, which is not a direct solution of the shallow water equations. For best results, however, the time series of a data set for filtering must exceed the period of the wave of interest to avoid spectral leakage (Wheeler & Weickmann, 2001). Furthermore, this filtering method can introduce spurious waves, when a certain signal shares a similar range of wavenumber and frequency with a wave of interest (Blanco, Nolan, & Mapes, 2016; Jung & Knippertz, 2023; S. N. Tulich & Kiladis, 2012; Yamasaki, 2011). In contrast, YP is suitable for real-time applications (Yang et al., 2021) as the projection is done instantaneously with only broad filtering to remove quasi-standing features. However, global fields of horizontal winds and geopotential are required, which restricts the use to analysis or model output fields with global coverage. As the projection is carried out using theoretical patterns, the MJO cannot be identified. Therefore, using both methods compensates for limitations of each and allows us to obtain a robust wave analysis (Knippertz et al., 2022).

While the terms EWs and convectively coupled equatorial waves are frequently used interchangeably, our approach explicitly identifies EWs via their dynamical signatures to subsequently investigate their coupling with convective proxies. When rainfall is utilized to isolate wave signals via the WK method, the resulting signal is inherently defined as a CCEW. In contrast, the YP projection method preserves the underlying dynamical structures regardless of convective state. Additionally, filtering wavenumber and frequency using convective proxies, such as rainfall, can introduce spurious waves, when a certain signal shares a similar range of wavenumber and frequency with a wave of interest. Such ambiguity is common in spectral filtering, where eastward-propagating superclusters may be conflated with convectively coupled KWs (Blanco, Nolan, & Mapes, 2016), or westward-propagating 2-day waves and African Easterly Waves may overlap with WIG1 (Jung & Knippertz, 2023; S. N. Tulich & Kiladis, 2012; Yamasaki, 2011). To mitigate these issues, we employ the complementary wave identification using both WK and YP methods and link them via the composite analysis (Section 2.3).

For WK, a zero-padding technique is used to avoid ringing effects. While a realistic simulation can be padded with observations (Janiga et al., 2018), here, the 40-day rainfall output is padded with 40-day zeros before and

after, such that the total length of the considered time series is 120 days. Furthermore, rainfall is averaged over 0–10°N, where the maximum rainfall is observed (Jung et al., 2023). The average over one hemisphere allows us to capture symmetric and antisymmetric components of waves without additional decomposition. Due to the 40-day analysis window, we focus our main discussion on Hovmöller diagrams of filtered rainfall, which can still capture the characteristics of the EWs. Although not a central part of this analysis, frequency-wavenumber power spectra are included in Supporting Information S1 (Figures S10 and S11) for interested readers.

For YP, a trapping scale y_0 is an important parameter. Due to the narrow channel geometry, we use y_0 of 5° instead of 6° as in many other studies (Ayesiga et al., 2022; Ferrett et al., 2020; Peatman et al., 2021). Finally, we use a composite technique to relate waves identified by the two approaches as in Jung and Knippertz (2023): Unfiltered rainfall is composited on the basis of the wave-filtered winds (YP), while unfiltered wind, temperature and humidity are composited on the basis of the wave-filtered rainfall (WK).

2.3. Composite Analysis for Kelvin Waves

To link KWs identified by the WK and YP approaches, we adopt a composite framework following Jung and Knippertz (2023). The key idea is to define the wave phase using filtered variables from one method and then composite unfiltered fields to diagnose the associated physical structures. Specifically, unfiltered rainfall is composited based on YP wave-filtered dynamical fields, whereas three-dimensional unfiltered winds, temperature, and specific humidity are composited based on WK wave-filtered rainfall.

Yang et al. (2021) described a general procedure to construct wave phase and amplitude using the YP method. In YP, each dynamical variable (e.g., zonal wind, meridional wind, and geopotential) is projected independently onto the theoretical horizontal structure of a given equatorial wave mode. Phase and amplitude are then defined using two variables that are in quadrature. This approach allows the temporal evolution of a wave to be represented from the perspective of a local observer as the wave propagates past a fixed longitude.

For many equatorial wave types, appropriate quadrature pairs consist of different dynamical variables sampled at different latitudes. For example, mixed Rossby–gravity waves can be characterized using meridional wind at the equator and zonal wind at an off-equatorial latitude (e.g., 10°N), consistent with their theoretical meridional structure. In aquachannel simulations, the off-equatorial latitude must be adjusted to account for the narrower meridional scale of the basic state. Similar selections are applied for equatorial Rossby and WIG1.

KWs, however, have no meridional wind component. Therefore, for KWs we define phase and amplitude using equatorial zonal wind u and its zonal gradient du/dx at 0°. From a local observer's perspective, an eastward-propagating KW is associated with a sequence of upper-level easterlies, upper-level convergence, upper-level westerlies, and upper-level divergence. When KWs are convectively coupled, upper-level divergence is typically accompanied by enhanced rainfall. To facilitate comparison among variables, all quantities used to define phase and amplitude are normalized by their standard deviation.

For the WK method, phase and amplitude are constructed using wave-filtered rainfall and its local tendency, following Riley et al. (2011), Yasunaga and Mapes (2012), and Schlueter et al. (2019). Both rainfall and its tendency are normalized by their standard deviation. From a local observer's perspective, the passage of a convectively coupled equatorial wave corresponds to increasing rainfall with a positive tendency, peak rainfall with near-zero tendency, and decreasing rainfall with a negative tendency.

Phase–amplitude space is discretized into eight equally spaced phases to examine the evolution of variables modulated by equatorial waves, while the four-phase framework was used by (Yang et al., 2021). For KWs identified by the YP method, the phase–amplitude diagram is constructed using normalized equatorial du/dx on the abscissa and normalized equatorial u on the ordinate, such that eastward propagation corresponds to clockwise rotation in phase space. For KWs identified by the WK method, the abscissa and ordinate are given by normalized rainfall and normalized rainfall tendency, respectively. The phases are numbered sequentially, with Phase 5 corresponding to maximum upper-level divergence in the YP framework and maximum rainfall in the WK framework.

Composites are constructed by averaging variables of interest within each phase. Only samples with amplitudes greater than 0.5 and smaller than 4.1 are retained, thereby excluding weak signals dominated by noise and rare extreme events. For example, unfiltered rainfall is composited based on YP-filtered KWs and then averaged

separately in each phase. This approach allows us to diagnose how dynamically identified KWs modulate precipitation and other unfiltered atmospheric fields.

2.4. Subjective Identification of Modes of Variability

2.4.1. Slowly Eastward-Propagating Disturbance

MJO-type disturbances are generally difficult to detect in our case because the typical timescale of 30–90 days is longer than our analysis period of 40 days. To overcome this, we identify the MJO-like signal subjectively through its characteristic propagation speed and fluctuations in outgoing longwave radiation (OLR), a widely used proxy for convection. The MJO produces large differences in OLR between its active and suppressed phase (Hendon & Salby, 1994; Roundy, 2012; Sobel & Kim, 2012). We identify the MJO-like signal through tracking regions of low unfiltered OLR averaged over 0°–10°N. To qualify a signal should propagate slowly eastward typical speeds around 5 m s^{-1}. We then composite variables of interest along the detected track, such as rainfall, horizontal wind, vertically integrated radiative fluxes and surface enthalpy fluxes. These composite fields are compared with realistic MJO characteristics from previous studies.

2.4.2. Quasi-Standing Waves

Most of the aquachannel simulations we conducted yield a relatively white spectrum of OLR, especially for periods longer than 20 days (not shown). We apply a space-time filter using a wavenumber window of 3–13 and a wave period of >20 days. This range of wavenumbers is applied to both east- and westward components. This wavenumber-frequency window allows us to capture slow-propagating and quasi-standing features. In order to capture quasi-standing waves, local minimum of the OLR along negative anomalies of filtered OLR is tracked at 6 hr intervals. The local minimum refers to a longitude band between 25°W and 25°E of the local minimum of the previous time stamp. After that, we composite moist static energy (MSE), temperature tendency due to radiation, zonal wind and other fields of interest on the basis of the identified standing waves.

3. Results

This section presents the main results of our aquachannel simulations. We begin with a discussion of the evolution of unfiltered fields of rainfall, zonal wind and OLR (Section 3.1). Section 3.2 focuses on KWs, identified as the most prominent EW in the aquachannel simulations. Next, we discuss the correspondence of a slowly eastward-propagating disturbance (SED) found in one of our simulations with the observed MJO (Section 3.3). Lastly, Section 3.4 characterizes the standing features observed in our simulations and discusses the underlying mechanisms.

3.1. Unfiltered Fields

We first explore Hovmöller diagrams of rainfall, OLR and zonal wind at 200 hPa without applying any filtering (Figure 1). The variables are averaged over 0–10°N to provide an unbiased view of propagating features while preserving the signal of any potential anti-symmetric wave modes. Note that averaging over other latitudinal bands (e.g., 15S–15°N or 0–10°S) shows no significant qualitative differences (not shown). The ICON model produces OLR from the radiation scheme, which corresponds to the upward radiative fluxes at the top of the atmosphere. A visual inspection of this figure shows an enormous range of variability patterns between the six different simulations, all with elements of eastward propagation at different speeds and standing or slowly drifting patterns. P13 (Figure 1a), in which both deep and shallow convection are parameterized, shows the largest variability of all runs revealing eastward propagation over a wide range of speeds (e.g., lines A–D) and some evidence of westward propagation with a reduced rainfall intensity of around 0.55 mm hr^{-1} (e.g., 20°E–0° from day 30 to 40). Lines A and B propagate at around 15 m s^{-1} and are associated with intense rainfall (Figure 1ai), OLR lower than 200 W m^{-2} (Figure 1aii), and easterlies to the west and westerlies to the east at 200-hPa (Figure 1aiii), indicative of strong upper-level divergence. Line C in contrast propagates eastward relatively fast (23–27 m s^{-1}) with moderate rainfall, OLR around 220 W m^{-2} and a marked increase of the upper-level westerlies that appear to propagate slightly faster than the other signals at a speed of 27 m s^{-1}. Finally, line D stands out as having the by far slowest propagation speed of only about 5 m s^{-1}. It emerges from a significant slow-down of line B around the "dateline" of the aquachannel. The associated rainfall is intense during the first about 10 days but then weakens and broadens in agreement with the OLR field. Interestingly, the upper-level

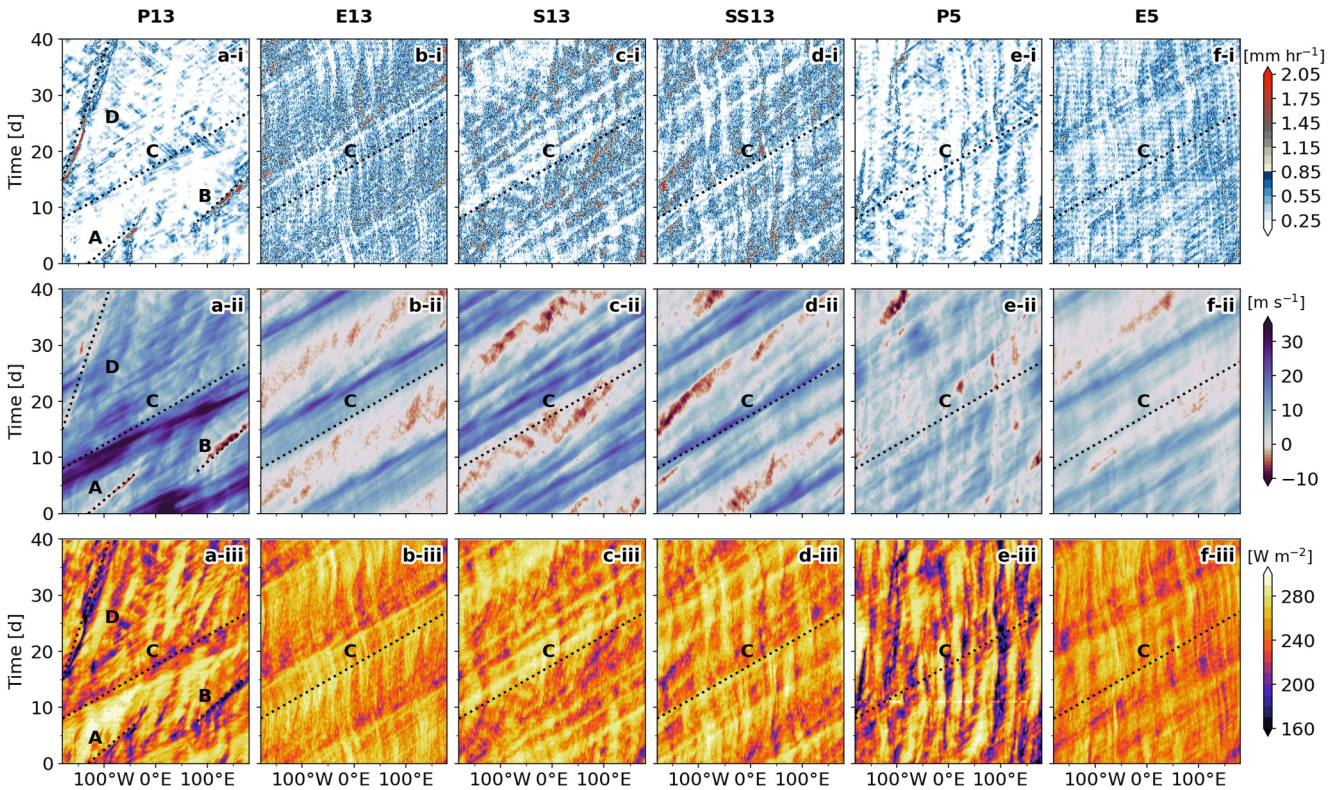

Figure 1. Hovmöller diagrams of (i) precipitation [mm h^{-1}], (ii) outgoing longwave radiation and (iii) zonal wind [m s^{-1}] at 200 hPa for each aquachannel simulation (Table 1). All fields are averaged over 0–10°N. The dotted lines indicate phase speeds of selected features. A: 17 m s^{-1}, B: 15 m s^{-1}, C: 24 m s^{-1}, and D: 5 m s^{-1}.

westerlies (Figure 1aiii) are weakened in the presence of this slowly propagating rainfall event. This goes along with a marked decrease in the variance of zonal wind at 200 hPa. When calculating the zonal variance of the wind field at each time step and averaging it over a time window, the variance in the first half of the simulation period is 74.6 m^2 s^{-2}, decreasing to 19.7 m^2 s^{-2} in the latter half. We will discuss these different behaviors of variability in more detail in Section 4.

The largest contrast to P13 is found in E13, in which both deep and shallow convection are explicitly represented (Figure 1b). Rainfall, zonal wind at 200 hPa and OLR are all dominated by a consistent eastward propagation (24 m s^{-1}) with a zonal wavenumber one. Compared to P13, there is much more widespread rainfall in E13, as this run generally produces more intense, localized rainfall events (Jung et al., 2023). Consistently, the variance of rainfall is significantly larger for E13 (0.067 mm^2 hr^{-2}) than for P13 (0.04 mm^2 hr^{-2}; Figure 2). Zonal wind at 200 hPa shows an alternating pattern of westerly and easterly flow (Figure 1biii), with an overall variance that is smaller in E13 (34.8 m^2 s^{-2}) than in P13 (55.0 m^2 s^{-2}; Figure 2). In addition to the large-scale wave motion, smaller-scale, more filamentary quasi-standing features of rainfall and OLR are noticeable that at times slowly drift eastward or westward. These are hardly discernible in the zonal wind at 200 hPa but clearer at 800 hPa (not shown). Spectral analysis of the OLR field reveals dominant quasi-standing waves characterized by a zonal wavenumber of 10 (not shown). Similar quasi-standing features in rainfall were found in the aquachannel and aquapatch runs of Blanco et al. (2019), who termed them S-shape phenomena. They demonstrated that quasi-standing features emerge from the interaction between superclusters and cloud clusters. Specifically, when a westward-propagating cloud cluster enters the domain of an eastward-moving supercluster, it is advected eastward; this motion is reversed as it exits the supercluster. A comparable behavior is evident in Figure 1bii, where smaller-scale filamentary structures shift to an eastward drift upon encountering a wavenumber-one structure.

S13 and SS13, which use explicit deep but parameterized shallow convection (Table 1), share similar patterns of rainfall, OLR and zonal wind at 200 hPa with those in E13 in terms of propagation speed and wavenumber (Figures 1c and 1d). The upper-level westerlies in S13 and SS13 (blue shading in Figures 1ciii and 1diii) exhibit a more pronounced wavenumber-one structure, which encompasses some narrow substructures also evident in E13.

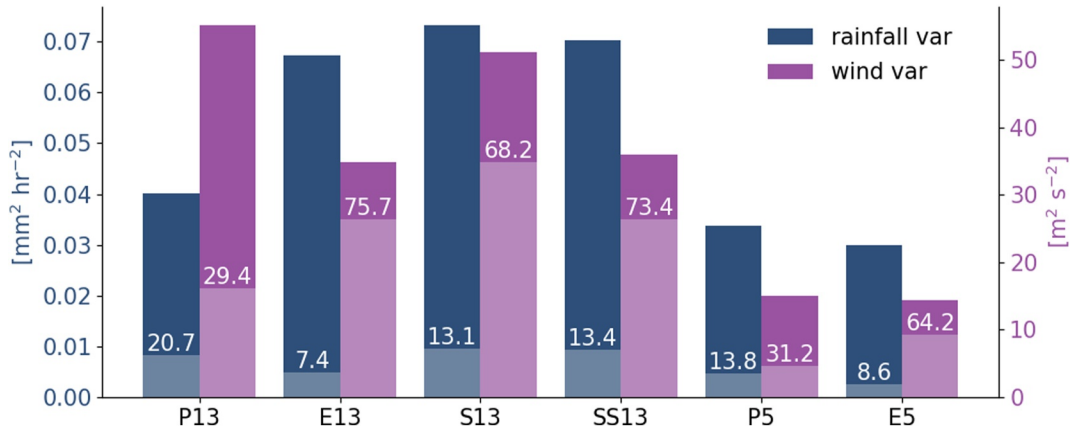

Figure 2. Total variances of rainfall and 200-hPa zonal wind in dark-colored bars, and variances of KW-filtered rainfall and KW-filtered zonal wind at 200 hPa in light-colored bars. The white numbers above the light-colored bars indicate the fraction of total variances explained by KWs in %, following the approach by Schlueter et al. (2019).

Beyond the wavenumber-one feature aligned with line C, the upper-level easterly packets (red shading) are distinct, which propagate slower than 24 m s^{-1}. Some propagating rainfall and OLR features substantially slow down and even evolve into a quasi-standing feature, for example, at around 80°E at day 18 in S13 and at 100°W at day 15 in SS13. These features potentially suggest an interaction between superclusters and cloud clusters (Blanco et al., 2019). Also, their zonal scale is characterized by a wavenumber of 10 as for E13. Another noticeable difference from E13 are the larger dry gaps in rainfall between the individual standing features (Figures 1ci and 1di). The wavenumber-one envelopes in zonal wind appear to contain slower moving easterly wind features, not evident in any of the other runs. S13 produces the largest rainfall variance and the second largest upper-level wind variance (Figure 2) of all simulations, showing that the treatment of shallow convection also influences deep convection and the upper-level dynamics.

Switching to a horizontal grid spacing of 5 km also changes the characteristics of variability. The differences are more noticeable between P13 and P5 than between E13 and E5. For the former, the wide spectrum of propagation speeds in P13 vanishes, leaving distinctive quasi-standing features in rainfall and OLR, and to a lesser extent, in zonal wind (Figure 1e). Furthermore, drifts of quasi-standing waves are less evident and eastward propagation happens only episodically. A zonal wavenumber of quasi-standing waves, which is identified using spectral analysis of OLR, is 8, which is smaller than in other explicit runs. The wind variance decreases by 73% from P13 (55 m^2 s^{-2}) to P5 (15 m^2 s^{-2}), while rainfall variance decreases rather little (Figure 2). Such effects of horizontal resolution on variability are surprising, given that P5 is initialized from the last time step of P13 with a spin-up of 3 days and horizontal grid spacing being the only difference between the two runs. We note, however, a potential limitation in this comparison. It cannot be ruled out that a similar reduction in variability would have eventually occurred in P13 had the analysis period been extended.

For explicit deep and shallow convection refining horizontal resolution from E13 to E5 creates overall smaller changes. Quasi-standing wave features with a zonal wavenumber of 10 in rainfall and OLR are also observed in E5 (Figures 1fi and 1fii) as in E13. An eastward propagating (speed of 24 m s^{-1}), wavenumber-one structure in rainfall, OLR and zonal wind at 200 hPa remains noticeable for E5 but less clear than E13. For explicit convection, refining horizontal resolution thus reduces the variances of rainfall and zonal wind by more than half (Figure 2). Note that some of this variance reduction may be attributed to the differing initial conditions and background states of E13 and E5, rather than horizontal resolution alone.

The overall response of tropical variability to horizontal resolution is somewhat counter-intuitive. While some global models show improvements in tropical variability with increasing horizontal resolution (Rackow et al., 2025; Rios-Berrios et al., 2022), our aquachannel simulations exhibit a reduction in rainfall and wind variances and a narrowing of the propagation spectrum. This suggests that the striking differences due to resolution change may not stem directly from small-scale processes, but rather from their cumulative impact on the mean state and large-scale circulation.

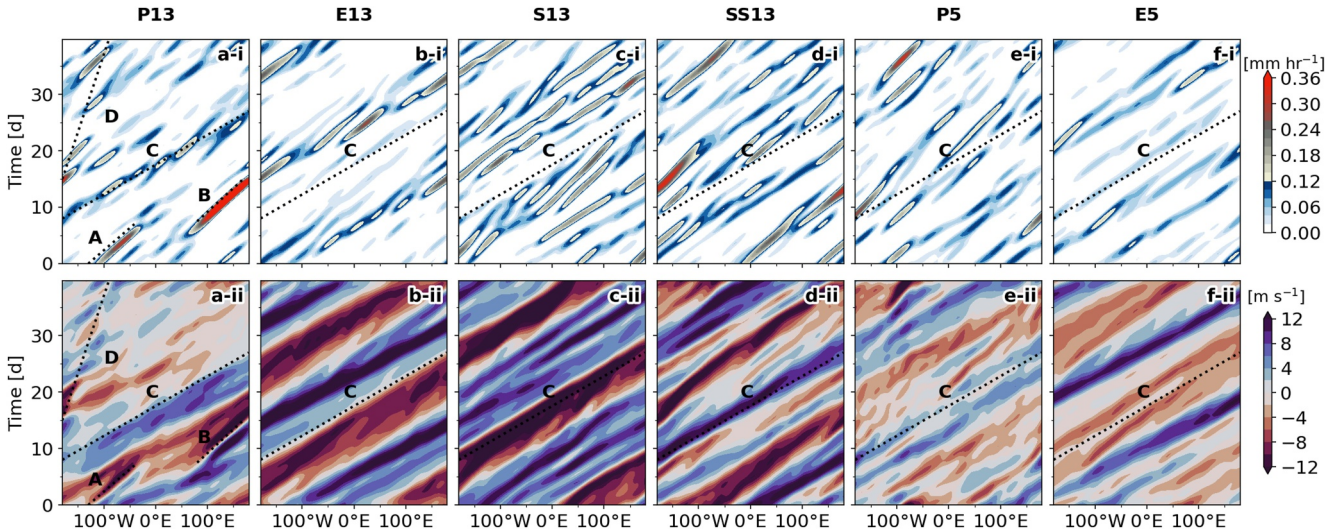

Figure 3. As in Figure 1 but for (i) KW-filtered rainfall [mm h^{-1}] using the WK method based on space-time filtering and (ii) KW-filtered zonal wind [m s^{-1}] at 200 hPa using the YP method based on spatial projection (see Section 2.2).

3.2. Kelvin Waves

3.2.1. Hovmöller Diagrams

A full wave analysis using the identification tools described in Section 2.2 reveals that Kelvin waves (KWs) are the most prominent EW type in all aquachannel simulations and thus, we focus the discussions on them here. Hovmöller diagrams of other wave types can be found in Figures S1 and S2 in Supporting Information S1 for completeness.

The eastward propagating features that we discussed in Section 3.1 are mostly consistent with KW-wave filtered fields (Figure 3). The clearest example is E13 (Figure 3b), where KW-filtered rainfall and zonal wind are dominated by a wavenumber-one eastward propagation with a phase speed of 24 m s^{-1}, similar to the unfiltered fields (Figure 1b). Looking at the KW-filtered rainfall signal at 180°W on day 15, for example, it is accompanied by KW-filtered westerlies at 200 hPa and easterlies at 850 hPa (the latter not shown), suggesting a first baroclinic structure. The easterly anomalies at low levels superpose with a mean easterly flow (Jung et al., 2023), which can enhance surface enthalpy fluxes and thus support the development of convection, a mechanism sometimes referred to as wind-induced surface heat exchange (WISHE; Emanuel, 1987; Neelin et al., 1987). The role of surface enthalpy fluxes will be discussed further using a composite analysis (Section 3.2.2). KWs explain the bulk (75.7%) of the total 200-hPa zonal wind variance in E13 (Figure 2). Their contribution to rainfall variability in contrast is rather small (7.4%), since this field is dominated by filamentary standing waves (Figure 1bi) and generally by short-lived, localized rainfall (Jung et al., 2023). This strongly suggest that while dynamics are dominated by KWs, rainfall is mostly controlled by thermodynamic processes.

KWs in S13 and SS13 (Figures 3c and 3d) share some similarities with E13. Both rainfall and wind are dominated by a zonal wavenumber one eastward propagation at 24 m s^{-1}, but rainfall patterns, and to some extent wind patterns in SS13, have more substructure with more slowly moving smaller-scale rainfall features. These are also evident in the unfiltered fields (Figures 1c and 1d). This hierarchical organization of slowly moving rainfall within a wavenumber-one packet is consistent with the interaction between the KW and the super cloud cluster (Blanco, Nolan, & Mapes, 2016). The interaction demonstrates that the convective envelope is composed of smaller-scale cloud clusters that propagate discontinuously or persist even as the faster-moving dynamical wave becomes uncoupled from the deep convection. The fraction of wind variability explained by KWs is marginally smaller for S13 (68.2%) and SS13 (73.4%) than for E13 (Figure 2). However, the role of KWs for rainfall variability becomes more important, explaining around 13% of the total rainfall variance (Figure 2).

The largest contrast to E13 is found for P13. Figure 3ai shows that the intense rainfall events marked as A and B coincide with KW-filtered rainfall. Upper-level westerlies and easterlies are observed to the east and west of the

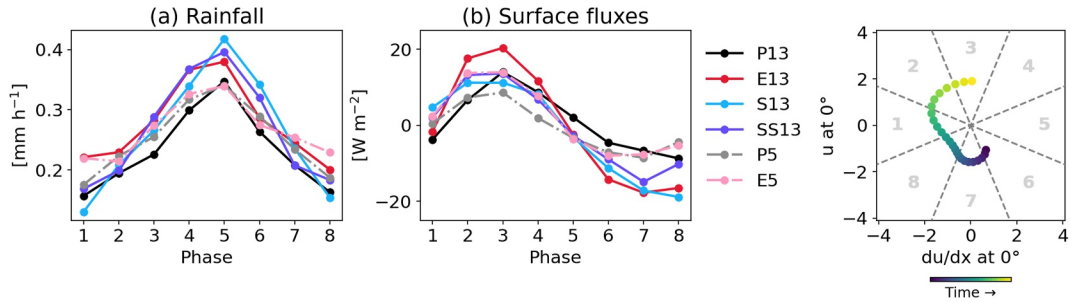

Figure 4. Composite of (a) unfiltered precipitation and (b) anomalies of surface enthalpy fluxes on the basis of eight KW phases as identified by the YP method. Composited variables are averaged over 0–10°N. Exemplary visualization is shown on the right to demonstrate how a composite analysis is constructed for a KW at a longitude at every 6 hr. Normalized divergence and zonal wind of KWs are denoted on the abscissa and ordinate axes, respectively. The inner and outer circles indicate when the amplitude of the amplitude is equal to standard deviations of 0.5 and 4.1, respectively. For example, a rainfall maximum would occur in Phase 5 where the upper-level divergence of KWs is large and the upper-level zonal wind associated with KWs is small.

event, respectively (Figure 3aii), indicating upper-level divergence. The fast propagating rainfall feature C (Figure 1ai) is also aligned with KW-filtered rainfall (Figure 3ai), encircling the entire channel with westerlies to the east but with a reduced amplitude of easterlies to the west (Figure 3aii). The slowly propagating rainfall feature D (Figure 1ai) is not associated with KW-filtered rainfall or zonal wind. Despite this, P13 has the highest fraction of total rainfall variance explained by KWs of 20.7% (Figure 2). In contrast, the contribution to wind variance is much smaller than for the other 13 km-runs hardly reaching 30%. As already discussed for the unfiltered wind field, the variance of KW-filtered zonal wind substantially decreases from the first to the second half of the simulation period (32.76 and 7.92 m^2 s^{-2}, respectively). This will further be discussed in Section 4.

Reducing the horizontal grid spacing from 13 to 5 km decreases the amplitudes of KWs in both rainfall and wind signals noticeably (Figures 3e and 3f), mainly due to the decreased total variances (Figure 2). This contrasts with previous studies, which demonstrated that the explicit representation of deep convection leads to enhanced rainfall associated with KWs (Rios-Berrios et al., 2022; Weber et al., 2021). Nevertheless, the importance of KWs for rainfall and wind variability is largely consistent with the coarse-resolution counterparts. P5 (Figure 3e) is dominated by rainfall signals propagating at 15 m s^{-1} with some moving faster (approx. 24 m s^{-1}). Wind structures tend to propagate faster and thus not always align well with the KW-filtered rainfall. Most of the rainfall signals are co-located with the upper-level divergence associated KWs, as seen for P13 (e.g., 0–100°E from day 20 to 30 and 125–50°W from day 30 to 40). For E5 (Figure 3f) both rainfall and zonal wind signals exhibit a consistent propagation speed of 24 m s^{-1}, as seen for E13. However, a wavenumber-one structure is less clear in the KW-filtered rainfall and the amplitudes are smaller (Figure 3fi).

3.2.2. Composite Analysis

Up to now, we have explored wave signals identified from rainfall and zonal wind at 200 hPa separately, using the two wave identification methods. To better demonstrate their relation, we use the phase-composited modulation of rainfall in eight phases of KWs identified by the YP method (Yang et al., 2003). All simulations (Figure 4a) show a rainfall maximum in Phase 5, as expected from theory. The maximum is greater for explicit deep convection at 13 km (E13, S13, SS13) than for the other runs, primarily because the former produce more intense rainfall in the ITCZ (Jung et al., 2023). A minimum rainfall occurs in Phase 1, which indicates the upper-level convergence of KWs, except for E13 where it is in Phase 8. Interestingly, the amplitude of the rainfall modulation is the smallest for explicit deep and shallow convection (E13 and E5), indicating a weak coupling between KW dynamics and convection.

Another interesting aspect of the rainfall modulation is that in E13, SS13, and E5 rainfall is substantially greater in Phase 4, that is, before the upper-level divergence of KWs than in Phase 6. Phase 4 indicates the westerly wind anomalies at 200 hPa and corresponding easterly wind anomalies at 850 hPa due to the first baroclinic structure of KWs. Given the fact that all simulations have the easterly mean in the lower troposphere (Jung et al., 2023), the

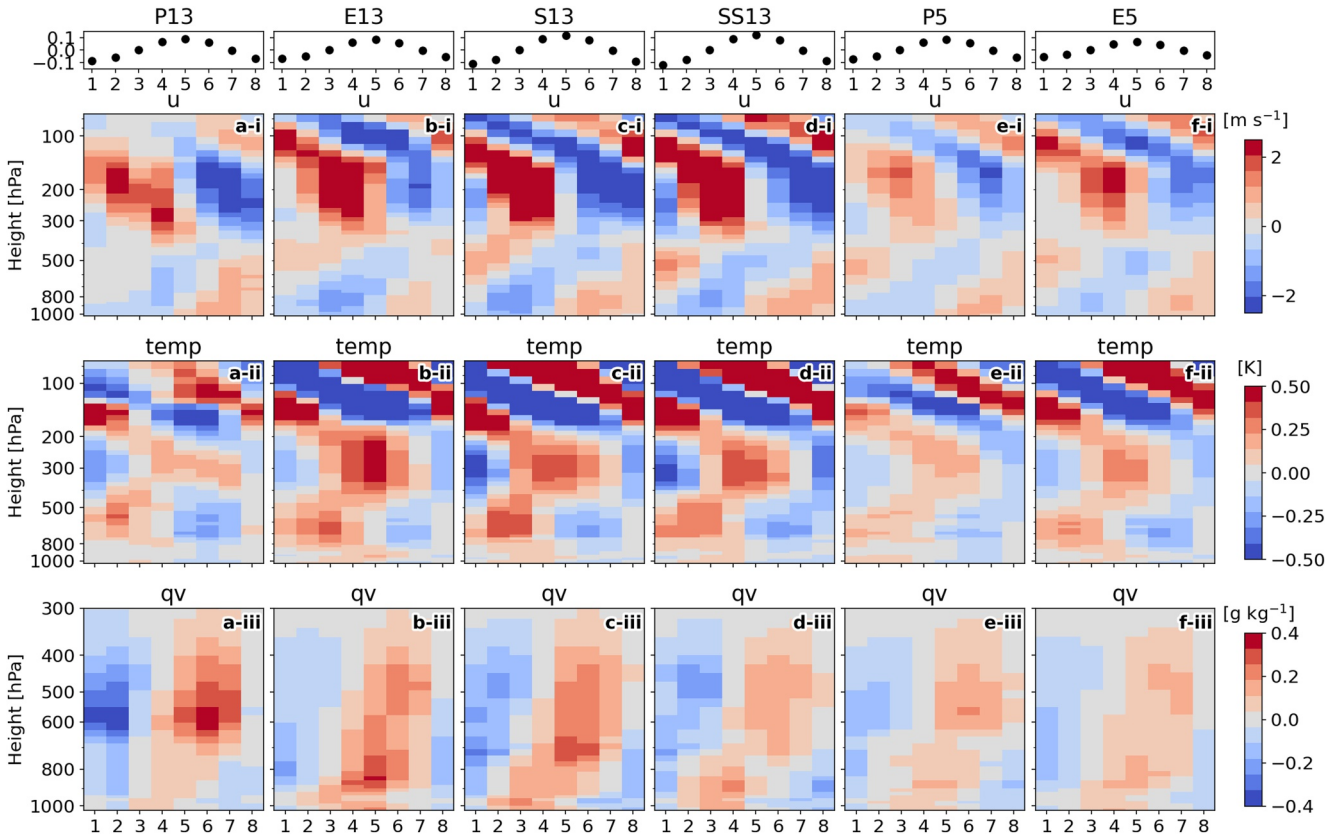

Figure 5. Composite of unfiltered anomalies of zonal wind (u), temperature (temp) and specific humidity (qv) on the basis of KW phases identified by the WK method for the six different simulations (Table 1). The uppermost panel shows normalized KW-filtered rainfall in each phase. Composited variables are averaged over 0–10°N. Note that the height in the lowest panel extends up to 300 hPa.

easterly wind anomalies at 850 hPa can lead to increased rainfall through WISHE. This wind-rainfall relation is also evident in Figure 3, and discussed in Section 3.2.1.

A corresponding analysis for surface enthalpy fluxes anomalies calculated from the time and zonal mean (Figure 4b) shows maxima around Phase 3, where the upper-level westerly (and corresponding low-level easterly) wind anomalies are large, and a minimum around the opposite Phase 7. This further corroborates that WISHE effects may help to support convection when going into the divergent wet phase. At the same horizontal resolution, explicit deep convection (E13, E5) produces a stronger surface enthalpy flux modulation than parameterized deep convection (P13, P5). It is conceivable that without a deep convection parameterization extra support from surface enthalpy fluxes is required to trigger convection. Furthermore, the enhanced flux modulation in E13 and E5 may be amplified by explicitly represented convective processes. More intense low-level evaporation of precipitation and subsequent surface layer cooling in these runs can increase the air-sea thermodynamic disequilibrium, thereby driving stronger enthalpy exchange than in the runs with parameterized deep convection.

Finally, we will analyze how the KW in the different simulations modulate the vertical structures in zonal wind, temperature and moisture (Figure 5). In contrast to Figure 4, composites are constructed here using the WK method applied to rainfall, which restricts us to convectively coupled KWs. The strongest modulation is found in E13 (Figure 5b). In the wet Phase 5, strong westerly wind anomalies are observed in the upper troposphere, followed by easterly wind anomalies, indicating upper-level divergence. Structures tilt above and below around 200 hPa, forming an elbow shape. The vertical structure of temperature shows warm anomalies in the lower troposphere before the wet phase, in the upper troposphere (and in the BL) during the wet phase, and strongly tilted large anomalies (±1.2 K) in the lower stratosphere. Moisture anomalies (Figure 5biii) begin at low levels before the wet phase and then rise throughout the troposphere with the largest moist anomaly at around 850 hPa in

Phase 5. Overall, these vertical structures are consistent with observed KW structures, except that the BL is rather cool in the wet phase in reality (Kiladis et al., 2009; Nakamura & Takayabu, 2022; Wheeler et al., 2000).

The other runs with explicit deep convection (S13 and SS13) closely follow E13 in terms of the vertical structures of zonal wind, temperature and humidity (Figures 5c and 5d). However, there are also some differences. For S13 and SS13, weak easterly anomalies at 200 hPa occur in the wet Phase 5, although the signature of the upper-level divergence is still evident with a sharp contrast of westerly and easterly anomalies. For temperature, differences from E13 are observed below 750 hPa, where anomalies are overall weaker. For humidity, S13 yields large anomalies at 700 hPa (Figure 5ciii), which is higher than E13. These small structural differences in zonal wind, temperature and humidity associated with KWs indicate that different shallow convection treatments marginally impact wave-convection coupling.

The largest differences from E13 are found in P13 (Figure 5a) with an overall weaker modulation by KWs. The zonal wind (Figures 5ai) has a less well defined elbow structure with weak westerly anomalies below 400 hPa and smaller wind anomalies in the lower stratosphere compared to E13. The temperature structure features lower-tropospheric warming before the wet phase and warming at 300 hPa during the wet phase, but warm anomalies are weaker than in E13, S13 and SS13. Furthermore, the mid-tropospheric warming is concentrated around 300 hPa for P13, while it is deeper for the other 13-km runs. Temperature anomalies in the tilted structure in the lower stratosphere are also substantially weaker (±1.2K in E13 vs. ±0.2K in P13), while both runs exhibit small anomalies below 800 hPa. For humidity (Figure 5aiii), anomalies have large values but are shifted to higher level around 600 hPa compared to the other runs.

Finally, the 5-km runs (Figures 5e and 5f) show reasonable KW modulations in agreement with E13, S13 and SS13 but with a smaller amplitude. P5 (Figure 5eii) shows that temperature anomalies in the BL become negative after the wet phase. Furthermore, the mid-troposphere warming in Phase 5 is more vertically expanded in P5 than in P13. In contrast, E5 (Figure 5fii) produces BL warming during the wet phase as seen in E13. For humidity, both 5-km runs (Figures 5eiii and 5fiii) exhibit positive humidity anomalies in the lower troposphere toward Phase 5, which later ascend up to the upper troposphere with a strong moistening at around 550 hPa (P5) and 450 hPa (E5). This ascending humidity anomaly with KW phase is largely consistent with Kiladis et al. (2009).

To summarize Section 3.2, KWs are the most prominent EW in all aquachannel simulations and substantially contribute to the variability of rainfall and zonal winds. Explicit deep convection (E13, S13, SS13 and E5) produces wavenumber-one KWs with a relatively consistent propagation speed of 24 m s^{-1}. For these runs, the upper-level wind variability is mainly controlled by KWs, contributing to more than 60% of the total wind variability, while their contribution to rainfall variability is weak (<15%). KWs in P13 and P5 propagate with varying speeds (15–24 m s^{-1}) with a reduced contribution of KWs to the total wind variability (approx. 30%). The composite analyses revealed that WISHE may play an important role for wave-convection coupling in E13, SS13 and E5, in the sense that enhanced surface fluxes help overcome high CIN to trigger convection with explicit deep convection. Furthermore, vertical structures of wind, temperature and humidity modulated by KWs largely agree with the observed structures.

3.3. Slowly Eastward-Propagating Disturbance

In Section 3.2 variability associated with KWs was discussed, but not the distinctive line D in P13 (Figure 1a), which propagates too slow for the WK filter (speed of only about 5 m s^{-1}) and does not project onto the KW structures assumed in YP. In other words, this slowly propagating feature does not have KW dynamical signatures. Visual inspection reveals that this feature shares similarities with the MJO in terms of propagation speed. To better bring out its meteorological characteristics, we track areas of low OLR along line D from day 15 to 40 in P13 (Figure 1aii) and construct composite fields on the basis of this track (Figure 6). Note that the longitude in Figure 6 extends only between 50°W and 50°E, which has a shorter wavelength than the real MJO (Lyu et al., 2021). Given the idealized model configuration and a simulation window that does not capture a full MJO lifecycle, this feature is treated as an illustrative case study rather than a direct analog of the real MJO. For clarity, we define this feature as a SED.

The SED is in phase with a maximum of precipitable water and rainfall (Figure 6a) stretching unusually far from the equator. This is in line with previous studies (Maloney & Hartmann, 1998; C. Zhang & Ling, 2012), claiming that off-equatorial flows associated with Rossby wave-induced moisture convergence lead to a broad rainfall

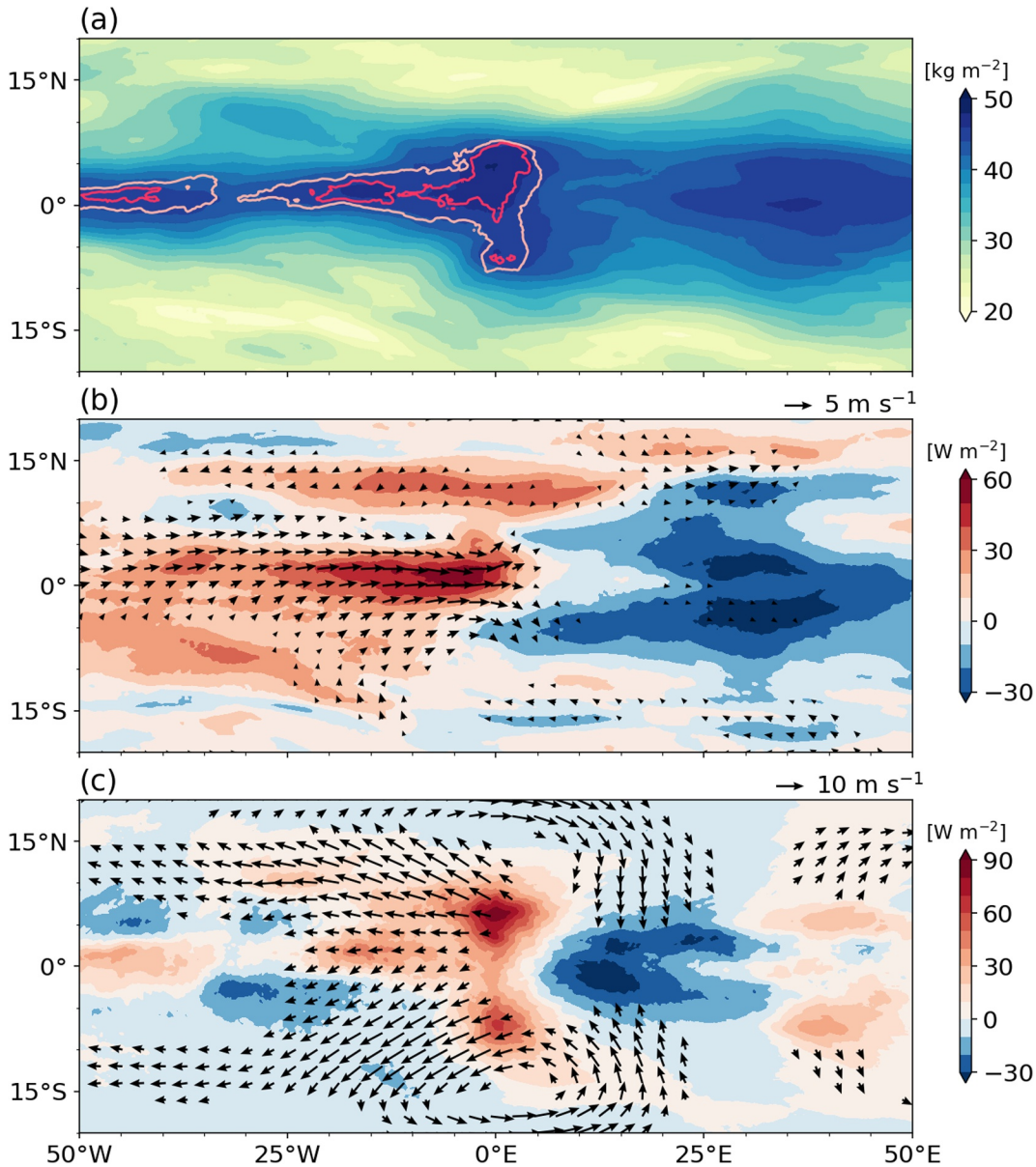

Figure 6. Composite fields of (a) precipitable water in shading and precipitation in contour (light and dark pink contours correspond to precipitation rates of 0.5 and 0.7 mm hr^{-1}, respectively), (b) anomalies of surface enthalpy fluxes in shading and anomalies of surface horizontal winds greater than 0.5 m s^{-1} in vectors, and (c) anomalies of column integrated longwave and shortwave radiative flux divergence in shading and anomalies of horizontal winds at 200 hPa greater than 2 m s^{-1} in vectors. The relative longitude of 0° indicates the outgoing longwave radiation minimum at each time step.

pattern (Salby et al., 1994). The maximum rainfall and precipitable water are more pronounced in the northern hemisphere than in the southern hemisphere. Given the symmetry of our model set-up, this must be largely a sampling issues, as the SED travels only a quarter of the entire tropics during our simulation period. The pattern also exhibits zonal asymmetry of precipitation with much greater rainfall on the western side (≥0.5 mm hr^{-1}) of the eastward-propagating disturbance, while the real MJO exhibits a smoother evolution of convection (C. Zhang & Ling, 2012). The composite surface pressure is also greater on the western side by 1.5 hPa (not shown). This is in line with C. Zhang (2005, their Figure 1), showing that low surface pressure is observed when enhanced convection associated with the MJO passes over the Maritime Continent and western Pacific. Around the center and on the western side, enhanced rainfall is co-located with high precipitable water in agreement with moisture mode theory (Adames & Maloney, 2021; Sobel & Maloney, 2012). To the east (30°–45°E), rainfall is low despite

a moist atmosphere. Although the patterns of rainfall and precipitation align with previous studies, enhanced rainfall indicates that the zonal scale of this disturbance is about 4,000 km. In contrast, the real-world MJO is defined as a planetary disturbance, typically ranging between 10,000 and 30,000 km (C. Zhang et al., 2020).

Figure 6b shows a sharp east-west contrast of surface flux anomalies with respect to the center of the SED. To the west of the reference point, positive anomalies of surface enthalpy fluxes are co-located with intensified surface wind anomalies. In contrast, wind anomalies are small on the eastern side, where surface flux anomalies are negative. This zonal asymmetry in surface enthalpy fluxes with surface winds indicates WISHE. Specifically, enhanced fluxes on the upwind side of the cluster favor upstream initiation of convection, which acts to slow the system's eastward propagation relative to pure advection by the mean flow (Emanuel, 1987). Surface winds hint at a pair of cyclonic Rossby gyres slightly lagged behind the SED. This pattern is, to some degree, consistent with the Matsuno-Gill model (Gill, 1980) and the skeleton model (Majda & Stechmann, 2009), which describe a dynamical structure of the MJO. In contrast, real-world observations reveal low-level easterlies preceding the convective envelope (Ling et al., 2013). The wind anomalies at 200 hPa (Figure 6c) are more prominent and reach further away from the equator, showing a pair of anticyclonic flows around the reference point and even ahead of it. These pronounced upper-level Rossby gyres likely facilitate the meridional transport of heat and momentum, potentially contributing to the evolution of the mean state and the wind variability observed during the latter half of P13 (Figure 1iii). This vertical tilt in the dynamical structure deviates from the stationary Matsuno-Gill model and is likely associated with the more complicated basic state and propagation.

Radiative flux divergence integrated throughout an atmospheric column (Figure 6c) provides insights into the net role of radiative warming or cooling. Positive anomalies of the column radiative flux divergence are nearly coincident with enhanced rainfall, while strong radiative cooling occurs at the leading edge of the SED. This relationship is consistent with findings of an observational study of the MJO (Lin & Mapes, 2004). A modeling study by Sobel and Maloney (2013) argued that anomalous radiative heating destabilizes the atmospheric column, supporting perturbation growth and thus helps maintain the MJO (Sobel & Maloney, 2013). This effect is modulated primarily through cloud-radiative feedbacks (Ciesielski et al., 2017), more specifically mostly high-level clouds (B. Zhang et al., 2019). In agreement with that, P13 produces more ice content (not shown) and exhibit much lower OLR (Figure 1aii), indicating higher cloud top than the explicit deep convection runs. Furthermore, cloud-radiative effects are an integral part of the moisture mode theory for the MJO.

3.4. Quasi-Standing Waves

In Sections 3.2 and 3.3 we explored propagating signals observed in the Hovmöller diagram of the unfiltered fields (Figure 1). In addition, there are pronounced quasi-standing features in unfiltered rainfall and OLR in all simulations, except for P13. The identification of quasi-standing waves is achieved through wavenumber-frequency filtering, providing the basis for tracking local OLR minima (see identified quasi-standing waves in Figure S3 in Supporting Information S1). We will explore these using again a composite analysis on the basis of low OLR (Section 2.4.2). We concentrate on results from P5 (Section 3.4.1) and E5 (Section 3.4.2), as the 13-km runs with explicit deep convection share similar behavior with E5. After that, we discuss the role of vertical advection, which is associated with maintaining quasi-standing waves in some runs (Section 3.4.3). The results of the 13-km runs are shown in Figures S4–S9 in Supporting Information S1.

3.4.1. Quasi-Standing Waves in P5

To detect the reasons for the formation of these quasi-standing waves, we will look at the MSE budget. MSE combines enthalpy of the dry air, gravitational potential energy and latent heat through condensation and evaporation and is conserved in moist adiabatic processes (Emanuel, 1994). As the horizontal distribution of temperature in the tropics is nearly homogeneous, a positive perturbation of MSE is usually associated with increased humidity and often moist convection. In fact, an MSE composite for quasi-standing waves in P5 (Figure 7a) exhibits positive anomalies co-located with the quasi-standing cloud features flanked by negative anomalies of similar magnitude about 20° to the west and east. The horizontal scale of quasi-standing waves is $\mathcal{O}$(1,000 km). This is larger than quasi-standing (or S-shape) cloud clusters in other aquachannel or aquapatch runs (Blanco et al., 2019) with horizontal scale of $\mathcal{O}$(100 km). The maximum anomalies are observed at 4 km height with the positive one slightly shifted to the west from the reference longitude 0°. Between the top of the BL and 4 km anomalies are tilted eastward with height, while above it anomalies are mostly upright extending up to

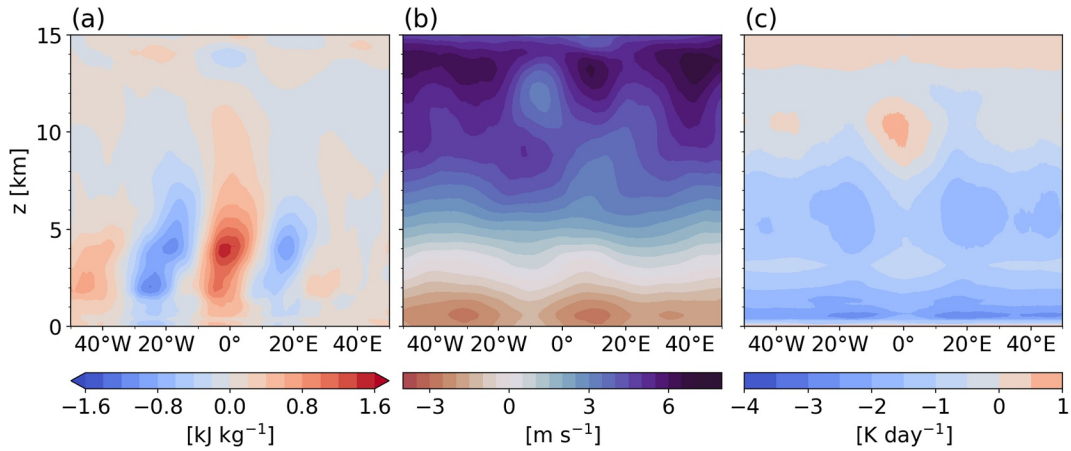

Figure 7. Composite fields of (a) anomalies of moist static energy [kJ kg^{-1}], (b) zonal wind [m s^{-1}], and (c) temperature tendency due to longwave and shortwave radiation [K d^{-1}] composited over the quasi-standing wave features in P5. Variables are averaged over 0°–10°N as in most other figures in this paper. The relative longitude of 0° indicates the center of a quasi-standing wave at each time step.

12 km. Around 14 km weak anomalies opposite to those in the mid-troposphere are found. Interestingly, the anomalies in the BL appear somewhat disconnected from the free-tropospheric ones with a broad positive signal around 0° and slightly weaker and narrower negative anomalies to the west and east.

To better understand these patterns, Figure 7b shows the corresponding zonal wind composite. Easterlies dominate below 4 km with a maximum near the surface at about 10° east of the OLR minimum, indicating a convergent inflow into the quasi-standing cloud feature. Above 4 km, westerlies of a magnitude increasing with height are found. A local maximum occurs at around 13 km above the near-surface wind maximum, indicating upper-level divergence out of the deep convection in the quasi-standing wave. The overall westerly shear is a possible explanation for the tilted MSE structures in the lower troposphere evident from Figure 7a. Looking at the vertical structure of the radiative heating (Figure 7c), here in absolute terms not anomalies, a prominent maximum is evident at around 10 km, mostly associated with the trapping of upwelling longwave radiative fluxes by thick anvil clouds with a high ice content ($>1.5\times10^{-2}$ g kg^{-1}, not shown). The radiative heating maximizes to the west of the reference longitude, showing an asymmetry with respect to the reference point. The cooling maxima up- and downstream of the heating peak around 6 km and close to the surface contribute to the negative MSE anomalies there (Figure 7a).

To understand which processes are important for modulating MSE, we consider the budget equation of the column integrated MSE and formulate the budget through anomalies from the time and zonal mean denoted as X':

$$\frac{\partial\langle h\rangle'}{\partial t} = -\langle u_h\cdot\nabla_h h\rangle' - \left\langle w\frac{\partial h}{\partial z}\right\rangle' + \langle Q_r\rangle' + F_h', \tag{1}$$

where h is MSE, u_h is the horizontal wind vector, w is the vertical velocity, Q_r is the longwave and shortwave radiative flux divergence and F_h is the surface enthalpy fluxes. The angle brackets denote a mass-weighted vertical integration, that is, $\langle X\rangle = \int \rho X dz$.

The MSE budget exhibits a significant residual in explicit deep convection runs, particularly within the ITCZ (not shown), where these runs exhibit more intense, more localized, shorter-lived rainfall in the ITCZ (Jung et al., 2023). This imbalance can be due to the fact that the 6-hourly sampling frequency is insufficient to resolve the life cycle of individual convective cells, which evolve on timescales of less than 1 hour. Furthermore, the coarsening of model grid to 0.2° lat-lon grid can introduce interpolation errors and smoothing of sharp horizontal gradients.

When plotting the four terms on the right-hand side of the MSE budget equation on a horizontal map (Figure 8), it is evident that the budget is dominated by a balance between radiation and horizontal advection. Positive

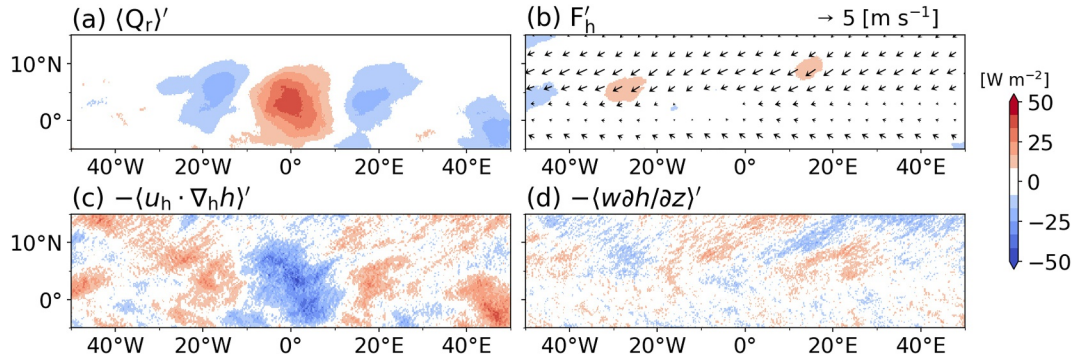

Figure 8. Composite fields of zonal and time anomalies of (a) column integrated total radiative flux divergence, (b) surface enthalpy fluxes, (c) column integrated horizontal advection of moist static energy (MSE) overlayed with horizontal surface wind vectors and (d) column integrated vertical advection of MSE. The relative longitude of 0° indicates the center of a quasi-standing wave at each time step. Note that the longitude extends between 50°W and 50°E and the latitude extends between 15°N and 5°S.

anomalies of $\langle Q_r' \rangle$ (Figure 8a) are found at reference longitude 0° with a maximum value of 40 W m^{-2}, shifted slightly into the northern hemisphere. This may be related to the fact that P5 is initialized from P13 characterized by the asymmetric SED (Figure 6). Asymmetry between the hemispheres is also evident in time and zonal mean rainfall (Figure 2 in Jung et al., 2023). Correspondingly, somewhat weaker negative anomalies are found about 20° to the west and east in accordance with the pattern seen in Figure 7a. Positive anomalies at the reference point are associated with radiative heating by anvil clouds (Figure 7c), which can induce an anomalous large-scale upward motion (C. Zhang et al., 2020).

The other source term in the MSE budget, F_h', does not appear to contribute much (Figure 8b) in contrast to the SED discussed above (Figure 6b). The surface wind field is dominated by off-equatorial easterly anomalies. Negative anomalies of $\langle u_h \cdot \nabla_h h \rangle'$ with some degree of noisiness (Figure 8c) compensate the radiative signal shown in Figure 8a, while there is an overall weak, noisy contribution from vertical advection (Figure 8d). The MSE and wind profiles (Figures 7a and 7b) indicate that in fact the MSE anomalies tend to occur in the layer of weakest wind and thus advection, with easterly (westerly) advection below (aloft). Taken together, these results suggest an initial generation of the quasi-standing features through convective and radiative processes similar to a moisture mode, which, however, shows little sign of growth or propagation due to balancing effects related to horizontal advection in the sheared background zonal flow.

3.4.2. Quasi-Standing Waves in E5

The corresponding analysis for E5 is shown in Figures 9 and 10, revealing some interesting similarities and differences. While the MSE anomalies have a similar east–west spacing with a horizontal scale of $\mathcal{O}$(1,000 km), the maximum is located much lower in E5, that is, around 2.5 km, and the tilt is predominantly from west to east with height (Figure 9a). This is consistent with the companion paper (Jung et al., 2023), who showed that the minimum of time and zonally averaged MSE is also located at a lower altitude for E5 than for P5. The zonal wind pattern (Figure 9b) bears great similarities to P5 but with a somewhat deeper easterly maximum to the east of the quasi-standing wave and less structure (and thus less divergence) in the westerlies aloft. As before, the vertical structure of the MSE anomaly is consistent with this zonal shear. Biggest and clearest difference is evident in radiative heating (Figure 9c). The composite shows very little east-west structure with net cooling everywhere apart from the highest levels above 13 km. Cooling maximizes immediately above the BL, and so possibly from low-level cloud tops, as well as in the mid-troposphere around 6 km. This strongly suggests a fundamentally different mechanism in E5 than P5 despite some structural similarities at first sight. We speculate that differences in the representation of anvil clouds between explicitly represented and parameterized convection schemes may play a significant role in determining the extent to which a moisture mode feedback can be realized in the model.

This speculation is further confirmed by the horizontal display of the budget terms for E5 (Figure 10). The radiative contribution indicated by $\langle Q_r \rangle'$ (Figure 10a) is dramatically reduced relative to P5 with a small positive signal to the center of the quasi-standing wave and hardly any considerable negative signals. Anomalies of F_h are

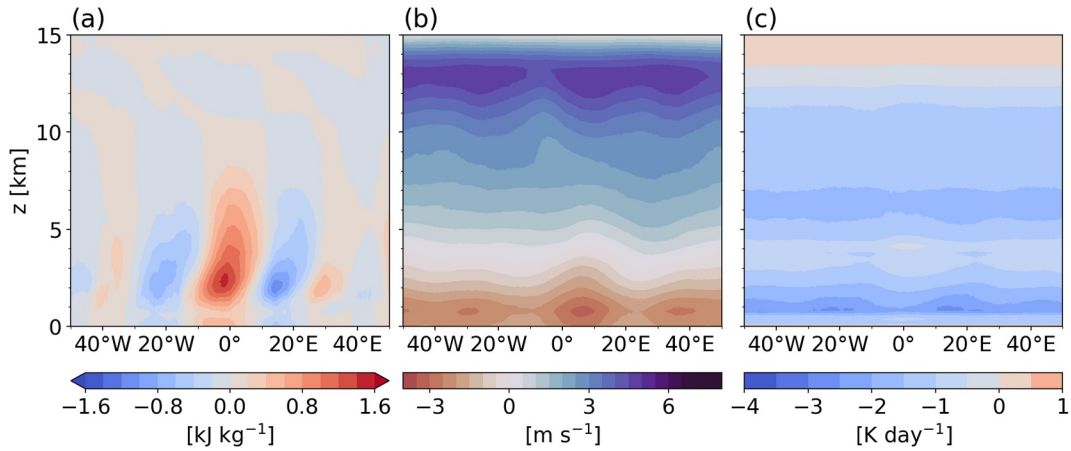

Figure 9. As in Figure 7 but for composite fields of quasi-standing waves in E5.

also small but at least show a weak dipole straddling the quasi-standing wave (Figure 10b). The consequence of this is that now the main balance occurs between horizontal and vertical advection. The former (Figure 10c) is in broad agreement with P5 but is more restricted to the northern hemisphere and overall much noisier, likely a result of the noisier explicit convection in E5. The latter (Figure 10d) is almost a mirror image but with an even higher level of noisiness. This behavior is also seen for the other runs with explicit deep convection at the coarser resolution (E13, S13 and SS13; see Figures S7–S9 in Supporting Information S1). These results suggest that vertical advection of MSE in explicitly represented deep convection can create quasi-standing waves that, once formed, can be balanced by horizontal advection in a shear background flow.

3.4.3. Role of Vertical Advection

We now want to understand why the column integrated vertical advection of MSE supports quasi-standing waves in E5, while it had more subtle effects in P5. The main ingredients to this quantity are the vertical profiles of MSE and vertical motion (Back & Bretherton, 2006; Inoue & Back, 2015). Assuming a typical MSE profile with a minimum in the mid-troposphere, a bottom-heavy vertical motion profile mostly transports high MSE from the low troposphere to the mid-troposphere, leading to a net import of MSE into the atmospheric column. In contrast, a top-heavy vertical motion profile transports low MSE from the mid-troposphere to the upper troposphere, leading to a net export of MSE. The net effect is, of course, also sensitive to the vertical profile of MSE, but that typically varies less. To disentangle the different contributions, we decompose vertical velocity and MSE into the zonal mean and the anomaly, that is, $X = \tilde{X} + X^*$. Then we vertically integrate the vertical advection terms and remove the time-zonal mean:

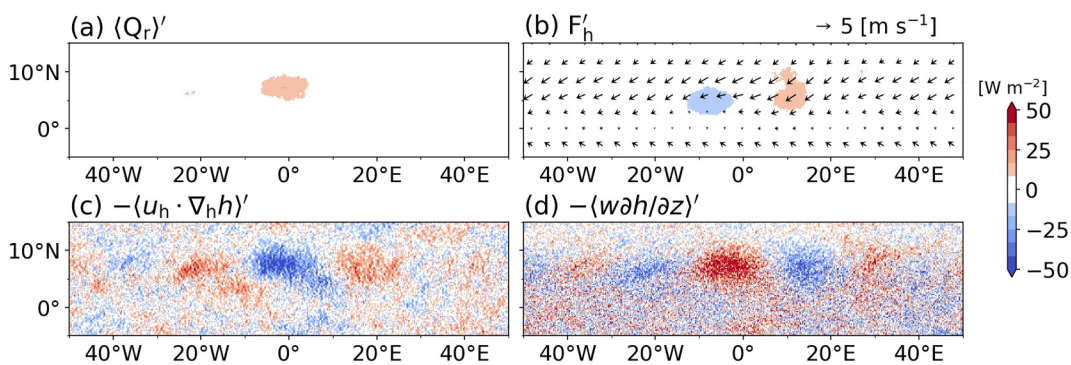

Figure 10. As in Figure 8 but for composite fields of quasi-standing waves in E5.

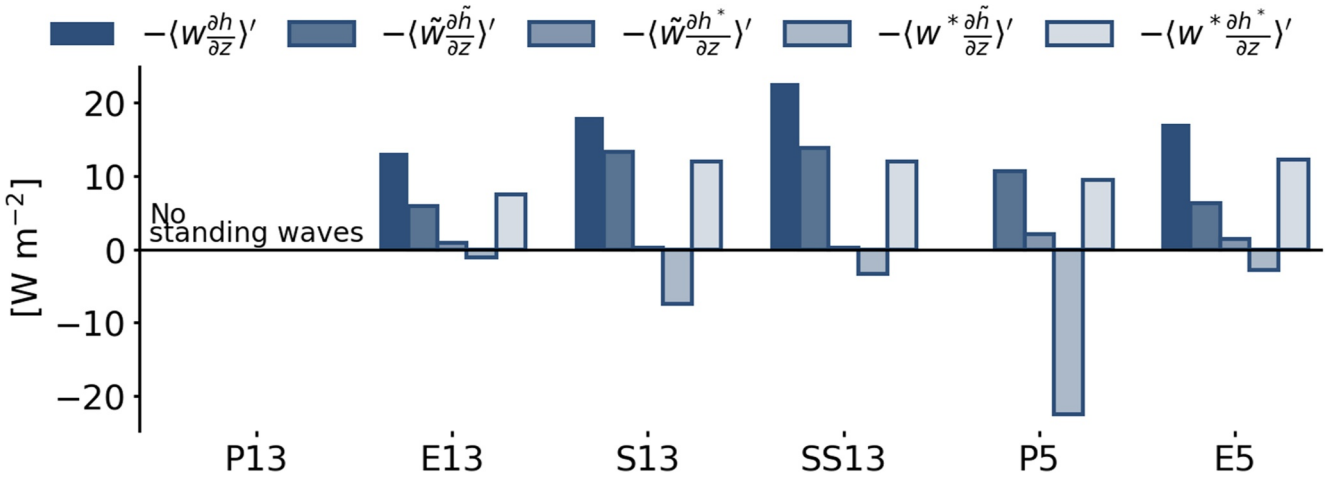

Figure 11. Area mean decomposition of the column integrated vertical advection of moist static energy (MSE) composited around quasi-standing waves and averaged over the area between 10°W–5°E and between 0°–10°N, that is where vertical advection acts as a source of MSE (Figure 10d). P13 is not shown because no quasi-standing waves are observed. Positive values of $-\langle X\rangle'$ imply a source of column integrated MSE.

$$\left\langle w\frac{\partial h}{\partial z}\right\rangle' = \left\langle \tilde{w}\frac{\partial \tilde{h}}{\partial z}\right\rangle' + \left\langle \tilde{w}\frac{\partial h^*}{\partial z}\right\rangle' + \left\langle w^*\frac{\partial \tilde{h}}{\partial z}\right\rangle' + \left\langle w^*\frac{\partial h^*}{\partial z}\right\rangle'. \quad (2)$$

In this framework, the background term $\langle \tilde{w}\frac{\partial \tilde{h}}{\partial z}\rangle'$ represents the advection of the zonal-mean MSE profile by the zonal-mean vertical motion. The thermodynamic term $\langle \tilde{w}\frac{\partial h^*}{\partial z}\rangle'$ captures how anomalous MSE stratification interacts with the background subsidence or ascent. The dynamic term $\langle w^*\frac{\partial \tilde{h}}{\partial z}\rangle'$ represents the effect of vertical motion acting on the background MSE profile. The eddy term $\langle w^*\frac{\partial h^*}{\partial z}\rangle'$ represents the interaction between local anomalies in both fields. We composite each term in Equation 2 around quasi-standing waves as in previous plots and average over the area between 10°W–5°E and between 0°–10°N, roughly corresponding to the region where the vertical advection term acts as a source of column integrated MSE (Figure 10d). To account for wave movement, one can easily rearrange the 2D vertically integrated terms relative to the wave center at each timestep, except for the background term $\langle \tilde{w}\frac{\partial \tilde{h}}{\partial z}\rangle'$. Computing the background term in the fixed domain with the moving wave center requires high-dimensional re-gridding before the vertical integration. Thus, the background term is derived as a residual in our study. While calculating the background term from the residual ensures internal consistency, we acknowledge it as a limitation, as it bundles potential numerical errors and unresolved physical interactions into the background component (Ren et al., 2021). A more rigorous explicit decomposition remains a target for future studies. Another note is that the vertical advection term contains model output w, which is computed differently between explicit and parameterized convection (Jung et al., 2023).

Figure 11 shows that for E5, the eddy term $\langle w^*\frac{\partial h^*}{\partial z}\rangle'$ of 12.3 W m^{-2} is the major contributor, followed by $\langle \tilde{w}\frac{\partial \tilde{h}}{\partial z}\rangle'$ of 6.3 W m^{-2}, while $\langle \tilde{w}\frac{\partial h^*}{\partial z}\rangle'$ and $\langle w^*\frac{\partial \tilde{h}}{\partial z}\rangle'$ make small positive and negative contributions of 1.4 and −2.8 W m^{-2}, respectively. As $\langle \tilde{w}\frac{\partial \tilde{h}}{\partial z}\rangle'$ is zonally averaged, this term indicates that the mean profiles of vertical motion and MSE are such that the resulting vertical advection acts as a source of MSE in the tropical belt (0°–10°N). At the same time, the leading contribution of $\langle w^*\frac{\partial h^*}{\partial z}\rangle'$ indicates that deviations of w and h from the zonal mean are essential for the column vertical advection in E5.

Comparison of E5 with the other simulations shows some interesting differences and similarities. E13 has a similar distribution of the decomposed terms and the value of $\langle \tilde{w}\frac{\partial \tilde{h}}{\partial z}\rangle'$ is comparable to E5, indicating that explicit deep and shallow convection creates a similar zonal mean effect of MSE and w irrespective of the difference in grid spacing. However, $\langle w^*\frac{\partial h^*}{\partial z}\rangle'$ in E13 is almost half the magnitude it has in E5 despite the fact that E13 produces the most intense and localized rainfall (Jung et al., 2023). This is because the range of values is larger in E13

(between −42 and 92 W m^{-2}) than for E5 (between −26 and 76 W m^{-2}) but averaging leads to substantial cancellation of terms with opposite signs.

For S13 and SS13, the term combining the two zonal means accounts for 13 W m^{-2}. This is more than double the contribution seen in E13 and E5. It suggests that the vertical mixing caused by shallow convection modifies the mean vertical profile of MSE in a way to strengthen the effect of vertical advection. There may also be effects on the mean vertical circulation as shown by C.-A. Chen et al. (2016). The term $\langle w^* \frac{\partial \bar{h}}{\partial z} \rangle'$ gains more importance as a sink, particularly in S13. This suggests that the zonal fluctuations of vertical motion act on a mean MSE profile in a way to dry out the atmosphere. The relatively large difference between S13 and SS13 is consistent with Sakradzija et al. (2020), who showed that a deterministic version of shallow convection parameterization (like S13) mixes the air between the boundary layer and the troposphere less efficiently than a stochastic version (like SS13). Part of this additional sink is compensated by a slightly more positive eddy term.

Lastly, P5 shows a distinctly different behavior. As for all others, the interaction of the two zonal means (10.6 W m^{-2}) and the eddy term $\langle w^* \frac{\partial h^*}{\partial z} \rangle'$ (9.4 W m^{-2}) act as sources of similar importance. These positive contributions, however, are offset by a large negative value of $\langle w^* \frac{\partial \bar{h}}{\partial z} \rangle'$ of −22.4 W m^{-2}, leading to a net vertical advection effect on MSE in P5 close to zero. The reasons for this surprising behavior may lie in the general characteristics of quasi-standing waves. As evident from Figure 1, quasi-standing waves in P5 have a larger zonal scale compared to the explicit convection runs with more pronounced dry areas between the bands. This suggests that the mean vertical gradient of MSE in P5 is more strongly controlled by subsidence, which leads to a drying and stabilization that in turn modifies effects of vertical advection by zonal fluctuations of vertical motion. Another potential factor is that w is computed differently in runs with parameterized convection, where convective up- and downdrafts within one grid cell can occur and cancel each other (Jung et al., 2023).

4. Discussion

After the thorough analysis of internal variability in Section 3, we would like to deepen the discussion here on two particularly interesting questions. In Section 4.1 we discuss why only P13 produces an SED, while Section 4.2 debates to what extent the quasi-standing waves found in our simulations are related to concepts of convective self-aggregation.

4.1. Distinct Behavior of P13

The planetary scale of the MJO is often attributed to cloud-radiative feedbacks generating instability in the atmospheric column, in particular high clouds (C. Zhang et al., 2020; B. Zhang et al., 2019). Section 3.3 showed that the SED in P13 does in fact exhibit positive anomalies of column radiative flux divergence coincident with intense rainfall and a large ice content. In P5, a similar cloud-radiative effect associated with anvil clouds is observed (Section 3.4), but here this mechanism supports quasi-standing waves rather than creating a planetary-scale, slowly propagating envelope like the MJO. Note that the SED in P13 is characterized more by a synoptic scale (several 1,000 km) than by a planetary scale. Interestingly, P5 is initialized with the last time step of P13, at which the SED is still present, and the spin-up period of P5 is only three simulation days. Since the MJO can usually be simulated when initial conditions already contain a large-scale feature (Maloney & Wolding, 2015), we anticipated a continuation but apparently this was not the case.

So how does horizontal resolution alone create the transition from a propagating large-scale disturbance to quasi-standing waves? Jung et al. (2023) showed that the mean states of P5 and P13 differ markedly as reflected in the strength of the Hadley circulation and the mean profile of zonal wind reproduced here in Figure 12. P13 noticeably deviates from the other simulations and exhibits the strongest vertical shear with strong westerlies of 13 m s^{-1} at 13 km. It is well known that the background zonal flow influences the dispersion of EWs and the MJO (Dias & Kiladis, 2014; S. Tulich & Kiladis, 2021), while vertical shear can affect the characteristics of equatorial Rossby waves (Wang & Xie, 1996), which have a great impact on simulating the MJO through their interaction with Kelvin waves (Barpanda et al., 2023). It is also known that MJO prediction skill is dependent on biases in a model's mean state (H. Kim et al., 2019). Additionally, variations in gross moist stability can modulate disturbance propagation, such that moderately negative gross moist stability combined with lower-level stretching has been shown to facilitate the slow eastward movement of large-scale convective vortices, while the disturbance becomes stationary under large negative gross moist stability (Figure 14 in M. Hayashi & Itoh, 2017). These

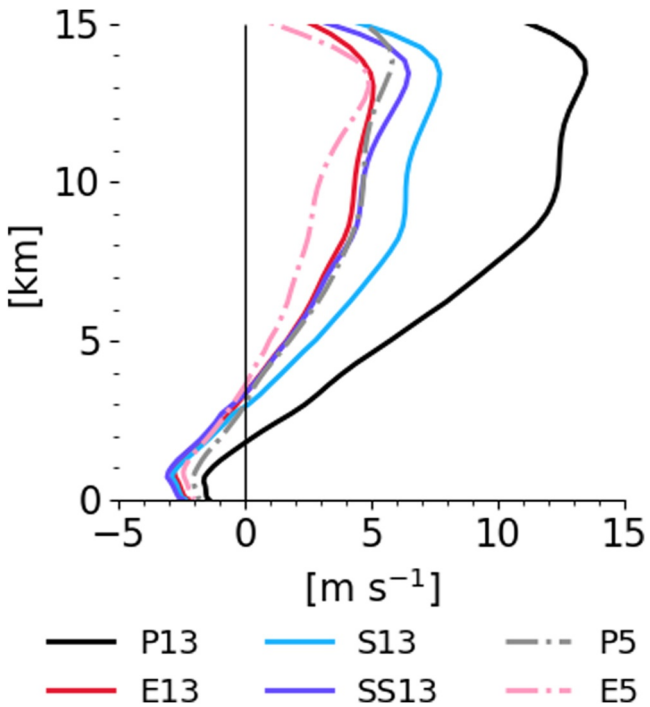

Figure 12. Profiles of zonal wind for the six different simulations averaged over the analysis period of 40 days and over the latitudinal belt between 0° and 10°N.

results suggest that the striking fundamental differences between P5 and P13 may not be a direct result of small-scale processes like convection and cloud-radiative effects per se but rather of their cumulative effects on the mean state and large-scale circulation in the two simulations. It can thus be regarded as yet another illustration of why it has been so challenging to represent the MJO in numerical models. While the analysis of the SED is limited by the single 40-day realization of P13, we present these results as a foundational case study. This work offers a valuable stepping stone for future research involving larger ensembles and longer simulation periods to fully explore the stochastic nature of the simulated MJO-like structure and conduct a robust analysis of its MSE budget.

It is remarkable that the SED appears only in P13 and despite the fact that our simulation setup uses zonally symmetric SSTs, which should isolate internal atmospheric mechanisms against the influence of zonal asymmetries like the Indo-Pacific warm pool (Das et al., 2019; H. Kim, 2024; H. Kim & Benedict, 2023). Interestingly, there are a number of other studies finding a slow-moving disturbance with zonally symmetric SSTs (Y.-Y. Hayashi & Sumi, 1986) and even with constant SST in an aquaplanet configuration (Arnold & Randall, 2015; Khairoutdinov & Emanuel, 2018). Although these hint at the atmosphere's intrinsic capacity to support intraseasonal modes, more work is needed to substantiate MJO-like disturbances in the absence of realistic SST distributions.

Lastly, Section 3.2 demonstrated that KWs becomes weaker when the SED is present in P13. This raises the question if this disturbance exists at the cost of KWs. The competition between KWs and the MJO is surprising, as some studies found that KW signals become in fact stronger during the active phase of the MJO (Baranowski et al., 2016; DePasquale et al., 2014; Roundy, 2008). While Sobel and Kim (2012) characterize the MJO-Kelvin transition as a process where the MJO accelerates and decouples into faster KWs as it moves eastward, our results show a transition from KWs into a SED. Furthermore, the SED also appears distinct from the circumnavigating mode described by Powell (2017) and F. Zhang et al. (2017), who view the MJO as a hybrid envelope that alternates between moisture waves and convectively coupled KWs. As the MJO-KW interaction appears to behave differently in our idealized simulation, further research using observations and modeling is required to unveil the reasons for this.

4.2. Quasi-Standing Waves and Convective Self-Aggregation

As discussed in Section 3, all simulations except P13 contain quasi-standing wave features. In some sense, these quasi-steady and quasi-stationary signatures are reminiscent of the concept of convective self-aggregation, that is spontaneous clustering of convective systems emerging from homogeneous initial conditions in RCE (Bretherton et al., 2005; Wing et al., 2020). As shown above, there is a fundamental difference between P5 and the runs with explicit deep convection (E13, S13, SS13 and E5). While in the former quasi-standing waves are kept stable by a balance of radiative effects and horizontal advection, the latter show weak radiative contributions but a more important role of vertical advection. The importance of vertical advection to strengthen shallow circulations in RCE has also been discussed by Coppin and Roehrig (2022). These fundamental differences, which are at least partly related to how ice clouds are treated in parameterized and explicit convection, also appear to influence the zonal scale of the quasi-standing waves, which are characterized by a zonal wavenumber of 8 in P5 and of 10 for the other runs. It is conceivable that the longwave cloud-radiative feedbacks operate at a somewhat larger scale than vertical advection. This is similar to the idea of the moisture mode theory claiming that cloud-radiative effects associated with anvil clouds play a crucial role in selecting the planetary scale of the MJO (B. Zhang et al., 2019).

5. Conclusions

Atmospheric variability in the tropics, including convectively coupled EWs and the MJO, controls tropical rainfall across various spatiotemporal scales and is considered a potential source of predictability. However, realistically simulating this variability is complex, and its representation is highly sensitive to model configuration. This manuscript compared the characteristics of atmospheric variability in tropical aquachannel simulations using the ICON NWP model. The simulations investigated differ in horizontal resolution (13 and 5 km) and treatment of deep and shallow convection. The channel geometry is designed with a zonal extension equivalent to the Earth's circumference and a meridional extension spanning from 30°N to 30°S, where time-invariant, zonally uniform variables are prescribed. The aquachannel geometry allows us to isolate tropical atmospheric dynamics by eliminating orography, land–sea contrasts, and tropical–extratropical interactions, while still permitting realistic zonal propagation of EWs. SSTs are also prescribed with a zonally symmetric distribution, peaking at the Equator (Jung et al., 2023).

All aquachannel simulations produce strong KWs dominating over other wave types. KWs show a wide range of speeds (15–24 m s^{-1}), when deep and shallow convection is parameterized at 13 km (P13), but are more uniform in the other simulations with a zonal wavenumber of one and a consistent propagation speed of around 24 m s^{-1}. In all simulations, KWs control substantial fractions of wind and rainfall variability. For example, KWs explain 20% of the total rainfall variability in P13 and more than 60% of zonal wind variability at 200 hPa in the runs with explicit deep convection.

Apart from KWs, there are two other interesting features of internal variability: an SED in P13 and quasi-standing waves in the other simulations. The processes relevant for each variability type are summarized in a schematic way in Figure 13. Quasi-standing waves, which are defined from a period of >20 days and local OLR minima, are sustained throughout the entire simulation period of 40 days and only drift slowly east- and westward. The underlying processes, however, vary between the runs with explicit deep convection and P5, where deep and shallow convection is parameterized at 5 km. For the former (Figure 13b), the vertical advection of MSE plays an important role to balance effects of horizontal advection between the quasi-standing features in a sheared zonal background flow. For the latter (Figure 13c), net effects of vertical advection are weak and cloud-radiative effects instead maintain the quasi-standing waves and appear to create larger zonal scales than in the other runs. We argue that this may due to a mechanism similar to the moisture mode theory for the MJO (B. Zhang et al., 2019). Broadly speaking, the quasi-standing waves show some similarity to ideas of convective self-aggregation but in a more realistic environment with planetary geometry, rotation, a Hadley circulation and sheared zonal flow.

P13 (Figure 13d) is the only simulation to produce a large-scale feature, which slowly propagates eastward at 5 m s^{-1}. Despite a somewhat shorter zonal wavelength, this feature resembles the MJO and is characterized by a pair of Rossby-gyres in the low- and upper-level horizontal wind fields. Moreover, it exhibits cloud-radiative effects similar to those associated with quasi-standing waves in P5. The fundamental difference between these two simulations is the mean-state circulation with a much stronger westerly background flow in P13. It demonstrates how differences in resolution (or convective treatment) can lead to differences at convective scale, which aggregate to shape different mean states, which in turn shape the larger-scale variability expressed through EWs, the MJO or quasi-standing waves.

As argued in previous studies, our manuscript corroborates that the representation of the tropical atmosphere is highly sensitive to model configuration (resolution, representation of shallow and deep convection), even in a simplified, zonally symmetric tropical aquachannel framework. Although the relatively high-resolution we use limits the number of realizations that we can perform and explore, we believe that the simulations illustrate fundamental characteristics of the tropical troposphere such as EWs, the MJO and convective self-aggregation, as well as challenges of how to best represent them in models. The idealized aquachannel configuration thereby allows us to study these phenomena in isolation from impacts of continents, topography, zonal SST gradients and the extratropics. An important next step now is to further explore how the different features identified here are also found in model simulations of full complexity and what that implies for weather forecasting and climate projections in the tropics.

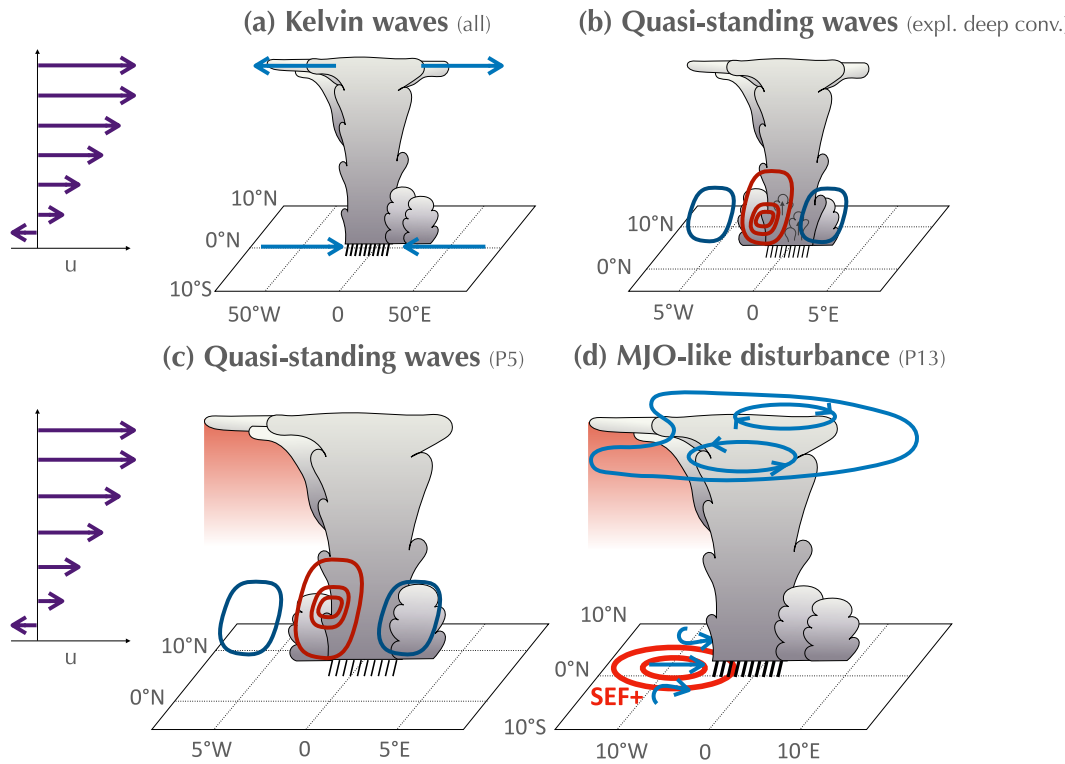

Figure 13. Schematic depiction of each variability type and associated processes with a feature-relative longitudinal and a realistic latitudinal scale. The profile of the zonal background wind is illustrated on the left. (a) KW-related rainfall is accompanied by upper-level divergence and low-level convergence (blue straight arrows). (b) In simulations with explicit deep convection, a balance of vertical and horizontal advection of moist static energy (MSE) sustains positive anomalous MSE (red contour lines). This positive anomaly is located slightly to the west of the center of quasi-standing waves and is flanked by negative anomalous MSE (blue contour lines). This process maintains the quasi-standing waves, which are embedded in the westerly background flow. (c) In P5, a balance of vertical advection and cloud-radiative effects (red shading) sustains positive anomalous MSE (red lines), maintaining quasi-standing waves with $\tilde{k}$. (d) An slowly eastward-propagating disturbance is maintained through interactions between a Matsuno-Gill circulation pattern (blue contour) and the combined diabatic effects of cloud-radiative feedback (red shading) and WISHE (red contour).

Conflict of Interest

The authors declare no conflicts of interest relevant to this study.

Availability Statement

Model output is published on Open Data LMU–Physics and available for download (Ruckstuhl et al., 2023). The analysis tools used in this paper are published on Zenodo at https://doi.org/10.5281/zenodo.20448695.

Acknowledgments
The research leading to these results has been done within the subproject "B6" of the Transregional Collaborative Research Center SFB/TRR 165 "Waves to Weather" (Craig et al., 2021), www.wavestoweather.de, funded by the German Research Foundation (DFG). Open Access funding enabled and organized by Projekt DEAL.

References

Adames, Á. F., & Kim, D. (2016). The MJO as a dispersive, convectively coupled moisture wave: Theory and observations. *Journal of the Atmospheric Sciences*, *73*(3), 913–941. https://doi.org/10.1175/JAS-D-15-0170.1

Adames, Á. F., & Maloney, E. D. (2021). Moisture mode theory's contribution to advances in our understanding of the Madden-Julian oscillation and other tropical disturbances. *Current Climate Change Reports*, *7*(2), 72–85. https://doi.org/10.1007/s40641-021-00172-4

Adames, Á. F., & Wallace, J. M. (2014). Three-dimensional structure and evolution of the MJO and its relation to the mean flow. *Journal of the Atmospheric Sciences*, *71*(6), 2007–2026. https://doi.org/10.1175/JAS-D-13-0254.1

Arnold, N. P., & Randall, D. A. (2015). Global-scale convective aggregation: Implications for the Madden-Julian oscillation. *Journal of Advances in Modeling Earth Systems*, *7*(4), 1499–1518. https://doi.org/10.1002/2015MS000498

Ayesiga, G., Holloway, C. E., Williams, C. J., Yang, G.-Y., Stratton, R., & Roberts, M. (2022). Linking equatorial African precipitation to kelvin wave processes in the CP4-Africa convection-permitting regional climate simulation. *Journal of the Atmospheric Sciences*, *79*(5), 1271–1289. https://doi.org/10.1175/JAS-D-21-0039.1

Back, L., & Bretherton, C. (2006). Geographic variability in the export of moist static energy and vertical motion profiles in the tropical Pacific. *Geophysical Research Letters*, *33*(17). https://doi.org/10.1029/2006GL026672

Baranowski, D. B., Flatau, M. K., Flatau, P. J., & Matthews, A. J. (2016). Impact of atmospheric convectively coupled equatorial kelvin waves on upper ocean variability. *Journal of Geophysical Research*, *121*(5), 2045–2059. https://doi.org/10.1002/2015JD024150

Barpanda, P., Tulich, S. N., Dias, J., & Kiladis, G. N. (2023). The role of subtropical Rossby waves in amplifying the divergent circulation of the Madden–Julian oscillation. *Journal of the Atmospheric Sciences*, *80*(10), 2377–2398. https://doi.org/10.1175/JAS-D-22-0259.1

Bauer, P., Thorpe, A., & Brunet, G. (2015). The quiet revolution of numerical weather prediction. *Nature*, *525*(7567), 47–55. https://doi.org/10.1038/nature14956

Bechtold, P., Köhler, M., Jung, T., Doblas-Reyes, F., Leutbecher, M., Rodwell, M. J., et al. (2008). Advances in simulating atmospheric variability with the ECMWF model: From synoptic to decadal time-scales. *Quarterly Journal of the Royal Meteorological Society*, *134*(634), 1337–1351. https://doi.org/10.1002/qj.289

Bengtsson, L., Dias, J., Gehne, M., Bechtold, P., Whitaker, J., Bao, J.-W., et al. (2019). Convectively coupled equatorial wave simulations using the ECMWF IFS and the NOAA GFS cumulus convection schemes in the NOAA GFS model. *Monthly Weather Review*, *147*(11), 4005–4025. https://doi.org/10.1175/MWR-D-19-0195.1

Bengtsson, L., Dias, J., Tulich, S., Gehne, M., & Bao, J.-W. (2021). A stochastic parameterization of organized tropical convection using cellular automata for global forecasts in NOAA's Unified forecast system. *Journal of Advances in Modeling Earth Systems*, *13*(1), e2020MS002260. https://doi.org/10.1029/2020MS002260

Blackburn, M., Williamson, D. L., Nakajima, K., Ohfuchi, W., Takahashi, Y. O., Hayashi, Y.-Y., et al. (2013). The aqua-planet experiment (APE): Control SST simulation. *Journal of the Meteorological Society of Japan*, *91*, 17–56. https://doi.org/10.2151/jmsj.2013-A02

Blanco, J. E., Nolan, D. S., & Mapes, B. E. (2016). Convectively coupled kelvin waves in aquachannel simulations: 2. Life cycle and dynamical-convective coupling. *Journal of Geophysical Research*, *121*(19), 11–319. https://doi.org/10.1002/2016JD025022

Blanco, J. E., Nolan, D. S., & Mapes, B. E. (2019). Nonlinear zonal propagation of organized convection in the tropics. *Journal of the Atmospheric Sciences*, *76*(9), 2837–2867. https://doi.org/10.1175/JAS-D-19-0082.1

Blanco, J. E., Nolan, D. S., & Tulich, S. N. (2016). Convectively coupled Kelvin waves in aquachannel simulations: 1. Propagation speeds, composite structures, and comparison with aquaplanets. *Journal of Geophysical Research*, *121*(19), 11–287. https://doi.org/10.1002/2016JD025004

Bretherton, C. S., Blossey, P. N., & Khairoutdinov, M. (2005). An energy-balance analysis of deep convective self-aggregation above uniform SST. *Journal of the Atmospheric Sciences*, *62*(12), 4273–4292. https://doi.org/10.1175/JAS3614.1

Bretherton, C. S., & Khairoutdinov, M. F. (2015). Convective self-aggregation feedbacks in near-global cloud-resolving simulations of an aquaplanet. *Journal of Advances in Modeling Earth Systems*, *7*(4), 1765–1787. https://doi.org/10.1002/2015MS000499

Chen, C.-A., Yu, J.-Y., & Chou, C. (2016). Impacts of vertical structure of convection in global warming: The role of shallow convection. *Journal of Climate*, *29*(12), 4665–4684. https://doi.org/10.1175/jcli-d-15-0563.1

Chen, S. S., Houze Jr, R. A., & Mapes, B. E. (1996). Multiscale variability of deep convection in relation to large-scale circulation in TOGA COARE. *Journal of the Atmospheric Sciences*, *53*(10), 1380–1409. https://doi.org/10.1175/1520-0469(1996)053⟨1380:MVODCI⟩2.0.CO;2

Ciesielski, P. E., Johnson, R. H., Jiang, X., Zhang, Y., & Xie, S. (2017). Relationships between radiation, clouds, and convection during DYNAMO. *Journal of Geophysical Research*, *122*(5), 2529–2548. https://doi.org/10.1002/2016JD025965

Coppin, D., & Bony, S. (2015). Physical mechanisms controlling the initiation of convective self-aggregation in a general circulation model. *Journal of Advances in Modeling Earth Systems*, *7*(4), 2060–2078. https://doi.org/10.1002/2015MS000571

Coppin, D., & Roehrig, R. (2022). Convection self-aggregation in CNRM-CM6-1: Equilibrium and transition sensitivity to surface temperature. *Journal of Advances in Modeling Earth Systems*, *14*(12), e2022MS003064. https://doi.org/10.1029/2022MS003064

Craig, G. C., Fink, A. H., Hoose, C., Janjić, T., Knippertz, P., Laurian, A., et al. (2021). Waves to weather: Exploring the limits of predictability of weather. *Bulletin of the American Meteorological Society*, *102*(11), E2151–E2164. https://doi.org/10.1175/BAMS-D-20-0035.1

Das, S., Sengupta, D., & Chakraborty, A. (2019). The Madden-Julian oscillation in an aquaplanet-like general circulation model with and without continents. *Journal of Advances in Modeling Earth Systems*, *11*(5), 1459–1476. https://doi.org/10.1029/2018MS001455

DePasquale, A., Schumacher, C., & Rapp, A. (2014). Radar observations of MJO and kelvin wave interactions during DYNAMO/CINDY2011/AMIE. *Journal of Geophysical Research*, *119*(11), 6347–6367. https://doi.org/10.1002/2013JD021031

Dias, J., Gehne, M., Kiladis, G. N., Sakaeda, N., Bechtold, P., & Haiden, T. (2018). Equatorial waves and the skill of NCEP and ECMWF numerical weather prediction systems. *Monthly Weather Review*, *146*(6), 1763–1784. https://doi.org/10.1175/mwr-d-17-0362.1

Dias, J., & Kiladis, G. N. (2014). Influence of the basic state zonal flow on convectively coupled equatorial waves. *Geophysical Research Letters*, *41*(19), 6904–6913. https://doi.org/10.1002/2014GL061476

Emanuel, K. A. (1987). An air-sea interaction model of intraseasonal oscillations in the tropics. *Journal of the Atmospheric Sciences*, *44*(16), 2324–2340. https://doi.org/10.1175/1520-0469(1987)044⟨2324:AASIMO⟩2.0.CO;2

Emanuel, K. A. (1994). *Atmospheric convection*. Oxford University Press on Demand.

Ferrett, S., Yang, G.-Y., Woolnough, S. J., Methven, J., Hodges, K., & Holloway, C. E. (2020). Linking extreme precipitation in Southeast Asia to equatorial waves. *Quarterly Journal of the Royal Meteorological Society*, *146*(727), 665–684. https://doi.org/10.1002/qj.3699

Gill, A. E. (1980). Some simple solutions for heat-induced tropical circulation. *Quarterly Journal of the Royal Meteorological Society*, *106*(449), 447–462. https://doi.org/10.1002/qj.49710644905

Grabowski, W. W. (2003). MJO-like coherent structures: Sensitivity simulations using the cloud-resolving convection parameterization (CRCP). *Journal of the Atmospheric Sciences*, *60*(6), 847–864. https://doi.org/10.1175/1520-0469(2003)060⟨0847:MLCSSS⟩2.0.CO;2

Haiden, T., Rodwell, M. J., Richardson, D. S., Okagaki, A., Robinson, T., & Hewson, T. (2012). Intercomparison of global model precipitation forecast skill in 2010/11 using the SEEPS score. *Monthly Weather Review*, *140*(8), 2720–2733. https://doi.org/10.1175/MWR-D-11-00301.1

Hayashi, M., & Itoh, H. (2017). A new mechanism of the slow eastward propagation of unstable disturbances with convection in the tropics: Implications for the MJO. *Journal of the Atmospheric Sciences*, *74*(11), 3749–3769. https://doi.org/10.1175/JAS-D-16-0300.1

Hayashi, Y.-Y., & Sumi, A. (1986). The 30-40 day oscillations simulated in an aqua planet model. *Journal of the Meteorological Society of Japan*, *64*(4), 451–467. https://doi.org/10.2151/jmsj1965.64.4_451

Hendon, H. H., & Salby, M. L. (1994). The life cycle of the Madden–Julian oscillation. *Journal of the Atmospheric Sciences*, *51*(15), 2225–2237. https://doi.org/10.1175/1520-0469(1994)051⟨2225:TLCOTM⟩2.0.CO;2

Holloway, C. E., Wing, A. A., Bony, S., Muller, C., Masunaga, H., L'Ecuyer, T. S., et al. (2017). Observing convective aggregation. *Surveys in Geophysics*, *38*(6), 1199–1236. https://doi.org/10.1007/s10712-017-9419-1

Holton, J. R. (2004). *An introduction to dynamic meteorology* (4th ed.). Elsevier Academic Press.

Inness, P. M., Slingo, J. M., Woolnough, S. J., Neale, R. B., & Pope, V. (2001). Organization of tropical convection in a GCM with varying vertical resolution; implications for the simulation of the Madden-Julian oscillation. *Climate Dynamics*, *17*(10), 777–793. https://doi.org/10.1007/s003820000148

Inoue, K., & Back, L. (2015). Column-integrated moist static energy budget analysis on various time scales during TOGA COARE. *Journal of the Atmospheric Sciences*, *72*(5), 1856–1871. https://doi.org/10.1175/JAS-D-14-0249.1

Janiga, M. A., Schreck, J. C., III, Ridout, J. A., Flatau, M., Barton, N. P., Metzger, E. J., & Reynolds, C. A. (2018). Subseasonal forecasts of convectively coupled equatorial waves and the MJO: Activity and predictive skill. *Monthly Weather Review*, *146*(8), 2337–2360. https://doi.org/10.1175/MWR-D-17-0261.1

Jiang, X., Adames, Á. F., Kim, D., Maloney, E. D., Lin, H., Kim, H., et al. (2020). Fifty years of research on the Madden-Julian Oscillation: Recent progress, challenges, and perspectives. *Journal of Geophysical Research*, *125*(17), e2019JD030911. https://doi.org/10.1029/2019JD030911

Judt, F. (2020). Atmospheric predictability of the tropics, middle latitudes, and polar regions explored through global storm-resolving simulations. *Journal of the Atmospheric Sciences*, *77*(1), 257–276. https://doi.org/10.1175/JAS-D-19-0116.1

Judt, F., & Rios-Berrios, R. (2021). Resolved convection improves the representation of equatorial waves and tropical rainfall variability in a global nonhydrostatic model. *Geophysical Research Letters*, *48*(14), e2021GL093265. https://doi.org/10.1029/2021GL093265

Jung, H., & Knippertz, P. (2023). Link between the time-space behavior of rainfall and 3D dynamical structures of equatorial waves in global convection-permitting simulations. *Geophysical Research Letters*, *50*(2), e2022GL100973. https://doi.org/10.1029/2022GL100973

Jung, H., Knippertz, P., Ruckstuhl, Y., Redl, R., Janjic, T., & Hoose, C. (2023). Understanding the dependence of mean precipitation on convective treatment and horizontal resolution in tropical aquachannel experiments. *Weather and Climate Dynamics*, *4*(4), 1111–1134. https://doi.org/10.5194/wcd-4-1111-2023

Jung, H., Naumann, A. K., & Stevens, B. (2021). Convective self–aggregation in a mean flow. *Atmospheric Chemistry and Physics*, *21*(13), 10337–10345. https://doi.org/10.5194/acp-21-10337-2021

Khairoutdinov, M. F., & Emanuel, K. (2018). Intraseasonal variability in a cloud-permitting near-global equatorial aquaplanet model. *Journal of the Atmospheric Sciences*, *75*(12), 4337–4355. https://doi.org/10.1175/JAS-D-18-0152.1

Kiladis, G. N., Wheeler, M. C., Haertel, P. T., Straub, K. H., & Roundy, P. E. (2009). Convectively coupled equatorial waves. *Reviews of Geophysics*, *47*(2). https://doi.org/10.1016/10.1029/2008RG000266

Kim, H. (2024). Decrease in MJO predictability following Indo–Pacific warm pool expansion. *Geophysical Research Letters*, *51*(13), e2024GL108849. https://doi.org/10.1029/2024GL108849

Kim, H., & Benedict, J. J. (2023). The idealized aquaplanet maritime continent barrier effect on the MJO predictability. *Journal of Climate*, *36*(17), 5757–5773. https://doi.org/10.1175/JCLI-D-22-0155.1

Kim, H., Janiga, M. A., & Pegion, K. (2019). MJO propagation processes and mean biases in the SubX and S2S reforecasts. *Journal of Geophysical Research*, *124*(16), 9314–9331. https://doi.org/10.1029/2019JD031139

Kim, H.-M., Webster, P. J., Toma, V. E., & Kim, D. (2014). Predictability and prediction skill of the MJO in two operational forecasting systems. *Journal of Climate*, *27*(14), 5364–5378. https://doi.org/10.1175/JCLI-D-13-00480.1

Knippertz, P., Gehne, M., Kiladis, G. N., Kikuchi, K., Rasheeda Satheesh, A., Roundy, P. E., et al. (2022). The intricacies of identifying equatorial waves. *Quarterly Journal of the Royal Meteorological Society*, *148*(747), 2814–2852. https://doi.org/10.1002/qj.4338

Lau, K., Nakazawa, T., & Sui, C. (1991). Observations of cloud cluster hierarchies over the tropical western Pacific. *Journal of Geophysical Research*, *96*(S01), 3197–3208. https://doi.org/10.1029/90JD01830

Li, Y., & Stechmann, S. N. (2020). Predictability of tropical rainfall and waves: Estimates from observational data. *Quarterly Journal of the Royal Meteorological Society*, *146*(729), 1668–1684. https://doi.org/10.1002/qj.3759

Lin, J.-L., & Mapes, B. E. (2004). Radiation budget of the tropical intraseasonal oscillation. *Journal of the Atmospheric Sciences*, *61*(16), 2050–2062. https://doi.org/10.1175/1520-0469(2004)061⟨2050:RBOTTI⟩2.0.CO;2

Ling, J., Zhang, C., & Bechtold, P. (2013). Large-scale distinctions between MJO and non-MJO convective initiation over the tropical indian ocean. *Journal of the Atmospheric Sciences*, *70*(9), 2696–2712. https://doi.org/10.1175/JAS-D-13-029.1

Lyu, M., Jiang, X., Wu, Z., Kim, D., & Adames, Á. F. (2021). Zonal-scale of the Madden-Julian Oscillation and its propagation speed on the interannual time-scale. *Geophysical Research Letters*, *48*(6), e2020GL091239. https://doi.org/10.1029/2020GL091239

Madden, R. A., & Julian, P. R. (1971). Detection of a 40–50 day oscillation in the zonal wind in the tropical Pacific. *Journal of the Atmospheric Sciences*, *28*(5), 702–708. https://doi.org/10.1175/1520-0469(1971)028⟨0702:DOAdoi⟩2.0.CO;2

Madden, R. A., & Julian, P. R. (1972). Description of global-scale circulation cells in the tropics with a 40–50 day period. *Journal of the Atmospheric Sciences*, *29*(6), 1109–1123. https://doi.org/10.1175/1520-0469(1972)029⟨1109:DOGSCC⟩2.0.CO;2

Majda, A. J., & Stechmann, S. N. (2009). The skeleton of tropical intraseasonal oscillations. *Proceedings of the National Academy of Sciences*, *106*(21), 8417–8422. https://doi.org/10.1073/pnas.0903367106

Maloney, E. D., & Hartmann, D. L. (1998). Frictional moisture convergence in a composite life cycle of the Madden–Julian oscillation. *Journal of Climate*, *11*(9), 2387–2403. https://doi.org/10.1175/1520-0442(1998)011⟨2387:FMCIAC⟩2.0.CO;2

Maloney, E. D., & Wolding, B. O. (2015). Initiation of an intraseasonal oscillation in an aquaplanet general circulation model. *Journal of Advances in Modeling Earth Systems*, *7*(4), 1956–1976. https://doi.org/10.1002/2015MS000495

Manabe, S., & Strickler, R. F. (1964). Thermal equilibrium of the atmosphere with a convective adjustment. *Journal of the Atmospheric Sciences*, *21*(4), 361–385. https://doi.org/10.1175/1520-0469(1964)021⟨0361:TEOTAW⟩2.0.CO;2

Mapes, B. E., & Houze, R. A., Jr. (1993). Cloud clusters and superclusters over the oceanic warm pool. *Monthly Weather Review*, *121*(5), 1398–1416. https://doi.org/10.1175/1520-0493(1993)121<1398:ccasot>2.0.co;2

Matsuno, T. (1966). Quasi-geostrophic motions in the equatorial area. *Journal of the Meteorological Society of Japan*, *44*(1), 25–43. https://doi.org/10.2151/jmsj1965.44.1_25

Miura, H., Satoh, M., Nasuno, T., Noda, A. T., & Oouchi, K. (2007). A Madden-Julian oscillation event realistically simulated by a global cloud-resolving model. *Science*, *318*(5857), 1763–1765. https://doi.org/10.1126/science.1148443

Nakajima, K., Yamada, Y., Takahashi, Y. O., Ishiwatari, M., Ohfuchi, W., & Hayashi, Y.-Y. (2013). The variety of spontaneously generated tropical precipitation patterns found in APE results. *Journal of the Meteorological Society of Japan*, *91*, 91–141. https://doi.org/10.2151/jmsj.2013-A04

Nakamura, Y., & Takayabu, Y. N. (2022). Convective couplings with equatorial Rossby waves and equatorial Kelvin waves. Part I: Coupled wave structures. *Journal of the Atmospheric Sciences*, *79*(1), 247–262. https://doi.org/10.1175/JAS-D-21-0080.1

Nakazawa, T. (1988). Tropical super clusters within intraseasonal variations over the western Pacific. *Journal of the Meteorological Society of Japan*, *66*(6), 823–839. https://doi.org/10.2151/jmsj1965.66.6_823

Neale, R. B., & Hoskins, B. J. (2000). A standard test for AGCMs including their physical parametrizations: I: The proposal. *Atmospheric Science Letters*, *1*(2), 101–107. https://doi.org/10.1006/asle.2000.0022

Neelin, J. D., Held, I. M., & Cook, K. H. (1987). Evaporation-wind feedback and low-frequency variability in the tropical atmosphere. *Journal of the Atmospheric Sciences*, *44*(16), 2341–2348. https://doi.org/10.1175/1520-0469(1987)044⟨2341:EWFALF⟩2.0.CO;2

Peatman, S. C., Schwendike, J., Birch, C. E., Marsham, J. H., Matthews, A. J., & Yang, G.-Y. (2021). A local-to-large scale view of Maritime Continent rainfall: Control by ENSO, MJO, and equatorial waves. *Journal of Climate*, *34*(22), 8933–8953. https://doi.org/10.1175/JCLI-D-21-0263.1

Powell, S. W. (2017). Successive MJO propagation in MERRA-2 reanalysis. *Geophysical Research Letters*, *44*(10), 5178–5186. https://doi.org/10.1002/2017GL073399

Prill, F., Reinert, D., Rieger, D., & Zängl, G. (2024). Icon tutorial: A comprehensive introduction to the icon modelling framework. *Deutscher Wetterdienst (DWD)*. Retrieved from https://www.dwd.de/DE/leistungen/nwv_icon_tutorial/pdf_einzelbaende/icon_tutorial2024.pdf

Privé, N. C., & Errico, R. M. (2013). The role of model and initial condition error in numerical weather forecasting investigated with an observing system simulation experiment. *Tellus*, *65*(1), 21740. https://doi.org/10.3402/tellusa.v65i0.21740

Rackow, T., Pedruzo-Bagazgoitia, X., Becker, T., Milinski, S., Sandu, I., Aguridan, R., et al. (2025). Multi-year simulations at kilometre scale with the integrated forecasting system coupled to FESOM2.5 and NEMOv3. 4. *Geoscientific Model Development*, *18*(1), 33–69. https://doi.org/10.5194/gmd-18-33-2025

Randall, D. A. (2013). Beyond deadlock. *Geophysical Research Letters*, *40*(22), 5970–5976. https://doi.org/10.1002/2013GL057998

Raymond, D. (2001). A new model of the Madden–Julian oscillation. *Journal of the Atmospheric Sciences*, *58*(18), 2807–2819. https://doi.org/10.1175/1520-0469(2001)058⟨2807:ANMOTM⟩2.0.CO;2

Raymond, D., Fuchs, Ž., Gjorgjievska, S., & Sessions, S. (2015). Balanced dynamics and convection in the tropical troposphere. *Journal of Advances in Modeling Earth Systems*, *7*(3), 1093–1116. https://doi.org/10.1002/2015MS000467

Ren, P., Kim, D., Ahn, M.-S., Kang, D., & Ren, H.-L. (2021). Intercomparison of mjo column moist static energy and water vapor budget among six modern reanalysis products. *Journal of Climate*, *34*(8), 2977–3001. https://doi.org/10.1175/JCLI-D-20-0653.1

Riley, E. M., Mapes, B. E., & Tulich, S. N. (2011). Clouds associated with the Madden–Julian oscillation: A new perspective from CloudSat. *Journal of the Atmospheric Sciences*, *68*(12), 3032–3051. https://doi.org/10.1175/JAS-D-11-030.1

Rios-Berrios, R., Bryan, G. H., Medeiros, B., Judt, F., & Wang, W. (2022). Differences in tropical rainfall in aquaplanet simulations with resolved or parameterized deep convection. *Journal of Advances in Modeling Earth Systems*, *14*(5), e2021MS002902. https://doi.org/10.1029/2021MS002902

Roundy, P. E. (2008). Analysis of convectively coupled Kelvin waves in the Indian Ocean MJO. *Journal of the Atmospheric Sciences*, *65*(4), 1342–1359. https://doi.org/10.1175/2007JAS2345.1

Roundy, P. E. (2012). Observed structure of convectively coupled waves as a function of equivalent depth: Kelvin waves and the Madden–Julian oscillation. *Journal of the Atmospheric Sciences*, *69*(7), 2097–2106. https://doi.org/10.1175/JAS-D-12-03.1

Ruckstuhl, Y., Janjić, T., Jung, H., Knippertz, P., & Redl, R. (2026). On the role of data assimilation in the prediction of tropical rainfall. *Monthly Weather Review*, *154*, 1337–1355. https://doi.org/10.1175/MWR-D-24-0129.1

Ruckstuhl, Y., Redl, R., Knippertz, P., Jung, H., & Janjic, T. (2023). Output data of idealised tropical channel simulations of an aqua planet at 5km and 13km resolution with icon for different convection conducts [Dataset]. *LMU Munich, Faculty of Physics*. https://doi.org/10.57970/P3AHB-YBA70

Sakradzija, M., Seifert, A., & Heus, T. (2015). Fluctuations in a quasi-stationary shallow cumulus cloud ensemble. *Nonlinear Processes in Geophysics*, *22*(1), 65–85. https://doi.org/10.5194/npg-22-65-2015

Sakradzija, M., Senf, F., Scheck, L., Ahlgrimm, M., & Klocke, D. (2020). Local impact of stochastic shallow convection on clouds and precipitation in the tropical Atlantic. *Monthly Weather Review*, *148*(12), 5041–5062. https://doi.org/10.1175/MWR-D-20-0107.1

Salby, M. L., Garcia, R. R., & Hendon, H. H. (1994). Planetary-scale circulations in the presence of climatological and wave-induced heating. *Journal of the Atmospheric Sciences*, *51*(16), 2344–2367. https://doi.org/10.1175/1520-0469(1994)051⟨2344:PSCITP⟩2.0.CO;2

Schlueter, A., Fink, A. H., Knippertz, P., & Vogel, P. (2019). A systematic comparison of tropical waves over northern Africa. Part I: Influence on rainfall. *Journal of Climate*, *32*(5), 1501–1523. https://doi.org/10.1175/JCLI-D-18-0173.1

Shi, X., Kim, D., Adames, Á. F., & Sukhatme, J. (2018). WISHE-moisture mode in an aquaplanet simulation. *Journal of Advances in Modeling Earth Systems*, *10*(10), 2393–2407. https://doi.org/10.1029/2018MS001441

Sobel, A., & Kim, D. (2012). The MJO-Kelvin wave transition. *Geophysical Research Letters*, *39*(20). https://doi.org/10.1029/2012GL053380

Sobel, A., & Maloney, E. (2012). An idealized semi-empirical framework for modeling the Madden–Julian oscillation. *Journal of the Atmospheric Sciences*, *69*(5), 1691–1705. https://doi.org/10.1175/JAS-D-11-0118.1

Sobel, A., & Maloney, E. (2013). Moisture modes and the eastward propagation of the MJO. *Journal of the Atmospheric Sciences*, *70*(1), 187–192. https://doi.org/10.1175/JAS-D-12-0189.1

Takayabu, Y. N. (1994). Large-scale cloud disturbances associated with equatorial waves Part I: Spectral features of the cloud disturbances. *Journal of the Meteorological Society of Japan*, *72*(3), 433–449. https://doi.org/10.2151/jmsj1965.72.3_433

Tiedtke, M. (1989). A comprehensive mass flux scheme for cumulus parameterization in large-scale models. *Monthly Weather Review*, *117*(8), 1779–1800. https://doi.org/10.1175/1520-0493(1989)117⟨1779:ACMFSF⟩2.0.CO;2

Tomassini, L. (2020). The interaction between moist convection and the atmospheric circulation in the tropics. *Bulletin of the American Meteorological Society*, *101*(8), E1378–E1396. https://doi.org/10.1175/BAMS-D-19-0180.1

Tompkins, A. M., & Craig, G. C. (1998). Radiative–convective equilibrium in a three-dimensional cloud-ensemble model. *Quarterly Journal of the Royal Meteorological Society*, *124*(550), 2073–2097. https://doi.org/10.1002/qj.49712455013

Tulich, S., & Kiladis, G. (2021). On the regionality of moist Kelvin waves and the MJO: The critical role of the background zonal flow. *Journal of Advances in Modeling Earth Systems*, *13*(9), e2021MS002528. https://doi.org/10.1029/2021MS002528

Tulich, S. N., & Kiladis, G. N. (2012). Squall lines and convectively coupled gravity waves in the tropics: Why do most cloud systems propagate westward? *Journal of the Atmospheric Sciences*, *69*(10), 2995–3012. https://doi.org/10.1175/JAS-D-11-0297.1

Vogel, P., Knippertz, P., Fink, A. H., Schlueter, A., & Gneiting, T. (2020). Skill of global raw and postprocessed ensemble predictions of rainfall in the tropics. *Weather and Forecasting*, *35*(6), 2367–2385. https://doi.org/10.1175/WAF-D-20-0082.1

Wang, B., & Xie, X. (1996). Low-frequency equatorial waves in vertically sheared zonal flow. Part i: Stable waves. *Journal of the Atmospheric Sciences*, *53*(3), 449–467. https://doi.org/10.1175/1520-0469(1996)053⟨0449:LFEWIV⟩2.0.CO;2

Weber, N. J., Kim, D., & Mass, C. F. (2021). Convection–kelvin wave coupling in a global convection-permitting model. *Journal of the Atmospheric Sciences*, *78*(4), 1039–1055. https://doi.org/10.1175/jas-d-20-0243.1

Wedi, N. P., Polichtchouk, I., Dueben, P., Anantharaj, V. G., Bauer, P., Boussetta, S., et al. (2020). A baseline for global weather and climate simulations at 1 km resolution. *Journal of Advances in Modeling Earth Systems*, *12*(11), e2020MS002192. https://doi.org/10.1029/2020MS002192

Wheeler, M., & Kiladis, G. N. (1999). Convectively coupled equatorial waves: Analysis of clouds and temperature in the wavenumber-frequency domain. *Journal of the Atmospheric Sciences*, *56*(3), 374–399. https://doi.org/10.1175/1520-0469(1999)056⟨0374:CCEWAO⟩2.0.CO;2

Wheeler, M., Kiladis, G. N., & Webster, P. J. (2000). Large-scale dynamical fields associated with convectively coupled equatorial waves. *Journal of the Atmospheric Sciences*, *57*(5), 613–640. https://doi.org/10.1175/1520-0469(2000)057⟨0613:LSDFAW⟩2.0.CO;2

Wheeler, M., & Weickmann, K. M. (2001). Real-time monitoring and prediction of modes of coherent synoptic to intraseasonal tropical variability. *Monthly Weather Review*, *129*(11), 2677–2694. https://doi.org/10.1175/1520-0493(2001)129⟨2677:RTMAPO⟩2.0.CO;2

Williamson, D. L., Blackburn, M., Nakajima, K., Ohfuchi, W., Takahashi, Y. O., Hayashi, Y.-Y., et al. (2013). The aqua-planet experiment (APE): Response to changed meridional SST profile. *Journal of the Meteorological Society of Japan*, *91*, 57–89. https://doi.org/10.2151/jmsj.2013-A03

Wing, A. A., Stauffer, C. L., Becker, T., Reed, K. A., Ahn, M.-S., Arnold, N. P., et al. (2020). Clouds and convective self-aggregation in a multimodel ensemble of radiative-convective equilibrium simulations. *Journal of Advances in Modeling Earth Systems*, *12*(9), e2020MS002138. https://doi.org/10.1029/2020MS002138

Yamasaki, M. (2011). Toward an understanding of the Madden-Julian oscillation: With a mesoscale-convection-resolving model of 0.2 degree grid. *Advances in Meteorology*, *2011*(1), 296914–296934. https://doi.org/10.1155/2011/296914

Yang, G.-Y., Ferrett, S., Woolnough, S., Methven, J., & Holloway, C. (2021). Real-time identification of equatorial waves and evaluation of waves in global forecasts. *Weather and Forecasting*, *36*(1), 171–193. https://doi.org/10.1175/WAF-D-20-0144.1

Yang, G.-Y., Hoskins, B., & Slingo, J. (2003). Convectively coupled equatorial waves: A new methodology for identifying wave structures in observational data. *Journal of the Atmospheric Sciences*, *60*(14), 1637–1654. https://doi.org/10.1175/1520-0469(2003)060⟨1637:CCEWAN⟩2.0.CO;2

Yasunaga, K., & Mapes, B. (2012). Differences between more divergent and more rotational types of convectively coupled equatorial waves. Part I: Space–time spectral analyses. *Journal of the Atmospheric Sciences*, *69*(1), 3–16. https://doi.org/10.1175/JAS-D-11-033.1

Ying, Y., & Zhang, F. (2017). Practical and intrinsic predictability of multiscale weather and convectively coupled equatorial waves during the active phase of an MJO. *Journal of the Atmospheric Sciences*, *74*(11), 3771–3785. https://doi.org/10.1175/JAS-D-17-0157.1

Zängl, G., Reinert, D., Rípodas, P., & Baldauf, M. (2015). The ICON (ICOsahedral Non-hydrostatic) modelling framework of DWD and MPI-M: Description of the non-hydrostatic dynamical core. *Quarterly Journal of the Royal Meteorological Society*, *141*(687), 563–579. https://doi.org/10.1002/qj.2378

Zhang, B., Kramer, R. J., & Soden, B. J. (2019). Radiative feedbacks associated with the Madden–Julian oscillation. *Journal of Climate*, *32*(20), 7055–7065. https://doi.org/10.1175/JCLI-D-19-0144.1

Zhang, C. (2005). Madden-julian oscillation. *Reviews of Geophysics*, *43*(2). https://doi.org/10.1029/2004RG000158

Zhang, C., Adames, Á., Khouider, B., Wang, B., & Yang, D. (2020). Four theories of the Madden-Julian oscillation. *Reviews of Geophysics*, *58*(3), e2019RG000685. https://doi.org/10.1029/2019RG000685

Zhang, C., & Ling, J. (2012). Potential vorticity of the Madden–Julian oscillation. *Journal of the Atmospheric Sciences*, *69*(1), 65–78. https://doi.org/10.1175/JAS-D-11-081.1

Zhang, F., Taraphdar, S., & Wang, S. (2017). The role of global circumnavigating mode in the MJO initiation and propagation. *Journal of Geophysical Research*, *122*(11), 5837–5856. https://doi.org/10.1002/2016JD025665